

Tracking Vector Magnetograms with the Magnetic Induction Equation

P. W. Schuck[†]

Plasma Physics Division, United States Naval Research Laboratory

4555 Overlook Ave., SW, Washington, DC 20375-5346

ABSTRACT

The differential affine velocity estimator (DAVE) developed in Schuck (2006) for estimating velocities from line-of-sight magnetograms is modified to directly incorporate horizontal magnetic fields to produce a differential affine velocity estimator for vector magnetograms (DAVE4VM). The DAVE4VM's performance is demonstrated on the synthetic data from the anelastic pseudospectral ANMHD simulations that were used in the recent comparison of velocity inversion techniques by Welsch et al. (2007). The DAVE4VM predicts roughly 95% of the helicity rate and 75% of the power transmitted through the simulation slice. Inter-comparison between DAVE4VM and DAVE and further analysis of the DAVE method demonstrates that line-of-sight tracking methods capture the shearing motion of magnetic footpoints but are insensitive to flux emergence — the velocities determined from line-of-sight methods are more consistent with horizontal plasma velocities than with flux transport velocities. These results suggest that previous studies that rely on velocities determined from line-of-sight methods such as the DAVE or local correlation tracking may substantially misrepresent the total helicity rates and power through the photosphere.

Subject headings: magnetic fields — Sun: atmospheric motions — methods: data analysis

1. Introduction

Coronal mass ejections (CMEs) are now recognized as the primary solar driver of geomagnetic storms (Gosling 1993). Several theoretical mechanisms have been proposed as drivers of CMEs, including large scale coronal reconnection (Sweet 1958; Parker 1957; Antiochos et al. 1999), emerging flux cancellation of the overlying coronal field (Linker et al. 2001), flux injection (Chen 1989, 1996), the kink instability of filaments (Rust & Kumar 1996; Török et al. 2004; Kliem et al. 2004), and photospheric footpoint shearing (Amari et al. 2000, 2003a,b; Schrijver et al. 2005). All of these CME mechanisms are driven by magnetic forces. The main differences depend on whether the magnetic helicity and energy are first stored in the corona and later released by reconnection and instability or whether the helicity and Poynting fluxes are roughly concomitant with the eruption. The timing and magnitude of the transport of magnetic helicity and energy through the photosphere provides an important discriminator between the mechanisms. In addition, eruption precursors in the photospheric magnetic field might provide reliable forecasting for space weather

[†]schuck@ppdmail.nrl.navy.mil

events. However, reliable, repeatable photospheric precursors of CMEs have so far eluded detection (Leka & Barnes 2003a,b, 2007).

The magnetic helicity and Poynting flux may be estimated from photospheric velocities inferred from a sequence of magnetograms (Berger & Ruzmaikin 2000; Démoulin & Berger 2003). However, accurately estimating velocities from a sequence of images is extremely challenging because image motion is ambiguous. The “aperture problem” occurs when different velocities produce image dynamics that are indistinguishable (Stumpf 1911; Marr & Ullman 1981; Hildreth 1983, 1984). Optical flow methods solve these under-determined or ill-posed problems that have no unique velocity field solution by applying additional assumptions about flow structure or flow properties. Both Schuck (2006) and Welsch et al. (2007) provide an overview of optical flow methods for recovering estimates of photospheric velocities from a sequence of magnetograms (Kusano et al. 2002, 2004; Welsch et al. 2004; Longcope 2004; Schuck 2005, 2006; Georgoulis & LaBonte 2006). Currently, most methods for estimating photospheric velocities implement some form of the normal component of the induction equation

$$\partial_t B_z + \nabla_h \cdot (B_z \mathbf{V}_h - V_z \mathbf{B}_h) = 0, \quad (1)$$

where the plasma velocity \mathbf{V} and the magnetic fields \mathbf{B} are decomposed into a local right-handed Cartesian coordinate system with vertical direction along the z -axis and the horizontal plane, denoted generically by the subscript “h,” containing the x - and y -axes.

Démoulin & Berger (2003) observed that the geometry of magnetic fields embedded in the photosphere implied that

$$\mathbf{F} = \mathbf{U} B_z \equiv B_z \mathbf{V}_h - V_z \mathbf{B}_h = \hat{\mathbf{z}} \times (\mathbf{V} \times \mathbf{B}) = \hat{\mathbf{z}} \times (\mathbf{V}_\perp \times \mathbf{B}), \quad (2a)$$

where \mathbf{F} denotes the flux transport vector, \mathbf{U} is the horizontal footpoint velocity or flux transport velocity ($\mathbf{U} \cdot \hat{\mathbf{z}} = 0$) and \mathbf{V}_\perp is the plasma velocity perpendicular to the magnetic field $\mathbf{V}_\perp \cdot \mathbf{B} = 0$. The flux transport vectors are composed of two terms $B_z \mathbf{V}_h$ and $V_z \mathbf{B}_h$ representing shearing due to horizontal motion and flux emergence due to vertical motion respectively. Equation (2a) may be used to transform (1) into a continuity equation for the vertical magnetic field

$$\partial_t B_z + \nabla_h \cdot (\mathbf{U} B_z) = 0, \quad (2b)$$

where plasma velocity may be written generally in terms of the flux transport velocity as

$$\mathbf{V} = \mathbf{U} - \frac{(\mathbf{U} \cdot \mathbf{B}_h) \mathbf{B}}{|\mathbf{B}|^2} + V_\parallel \frac{\mathbf{B}}{|\mathbf{B}|}, \quad (3a)$$

$$\mathbf{V}_{\perp h} = \mathbf{U} - \frac{(\mathbf{U} \cdot \mathbf{B}_h) \mathbf{B}_h}{|\mathbf{B}|^2}, \quad (3b)$$

$$\mathbf{V}_{\perp z} = -\frac{(\mathbf{U} \cdot \mathbf{B}_h) \mathbf{B}_z}{|\mathbf{B}|^2}, \quad (3c)$$

and the subscripts “ \parallel ” and “ \perp ” denote plasma velocities parallel and perpendicular to the magnetic field respectively. Equations (3a-c) are the algebraic decomposition (Welsch et al. 2004) generalized for arbitrary parallel velocity V_\parallel , but the value of V_\parallel does not affect the perpendicular plasma velocity (3b)-(3c) or the perpendicular electric field

$$c \mathbf{E}_\perp = -\mathbf{V} \times \mathbf{B} = -\overbrace{\mathbf{U} \times \hat{\mathbf{z}} B_z}^{\mathbf{E}_{\perp h}} - \overbrace{\mathbf{U} \times \mathbf{B}_h}^{\mathbf{E}_{\perp z}}, \quad (4)$$

which both depend only on the flux transport velocity \mathbf{U} .

Equations (1)-(3) should be formally distinguished from the *inverse problem* for determining an estimate of the plasma velocity \mathbf{v} from vector magnetograms using the normal component of the magnetic induction equation

$$\partial_t B_z + \nabla_h \cdot (B_z \mathbf{v}_h - v_z \mathbf{B}_h) = 0, \quad (5a)$$

where

$$\mathbf{f} = \mathbf{u} B_z = B_z \mathbf{v}_h - v_z \mathbf{B}_h = \hat{\mathbf{z}} \times (\mathbf{v} \times \mathbf{B}) = \hat{\mathbf{z}} \times (\mathbf{v}_\perp \times \mathbf{B}), \quad (5b)$$

and the *inverse problem* for determining flux transport velocity \mathbf{u} from the evolution of the vertical magnetic field or line-of-sight component

$$\partial_t B_z + \nabla_h \cdot (\boldsymbol{\vartheta} B_z) = 0. \quad (6)$$

The notation $\boldsymbol{\vartheta}$, denoting an optical flow estimate, emphasizes that $\boldsymbol{\vartheta}$ determined from (6) is not necessarily immediately identified with the flux transport velocity \mathbf{u} . Equations (5)-(6) are ill-posed inverse problems because of two ambiguities:

1. The Helmholtz decomposition of the flux transport vectors (Welsch et al. 2004; Longcope 2004)

$$\mathbf{f} = \mathbf{u} B_z = B_z \mathbf{v}_h - v_z \mathbf{B}_h = -(\nabla_h \phi + \nabla_h \psi \times \hat{\mathbf{z}}), \quad (7)$$

where ϕ is the inductive potential and ψ is the electrostatic potential manifestly demonstrates that only inductive potential ψ may be unambiguously determined from the local evolution of B_z in (5). The electrostatic potential ϕ must be constrained by additional assumptions. By analogy, (6) is also ill-posed for the same reason; $\nabla_h \times (\boldsymbol{\vartheta} B_z)$ is not constrained by the local evolution of $\partial_t B_z$.

2. For (5a) and (5b) V_\parallel is not constrained by the local evolution of $\partial_t B_z$. For (6), there is no *a priori* relationship between $\boldsymbol{\vartheta}$ and \mathbf{u} or $\boldsymbol{\vartheta}$ and \mathbf{v} for the inverse problem. However, if $\boldsymbol{\vartheta}$ is identified with the flux transport velocity \mathbf{u} then \mathbf{u} and \mathbf{v} will satisfy the same relationships as \mathbf{U} and \mathbf{V} in (3).

The first ambiguity may be resolved for (5a) by the induction method (IM) (Kusano et al. 2002, 2004), minimum energy fit (MEF) (Longcope 2004), or the differential affine velocity estimator for vector magnetograms (DAVE4VM) presented in § 2. These methods produce *a unique solution* for \mathbf{v} , but not necessarily *the unique solution* that corresponds to \mathbf{V} . The first ambiguity may be resolved for (6) by local optical flow methods such as the differential affine velocity estimator (DAVE) (Schuck 2006), its nonlinear generalization (Schuck 2005), global methods (Wildes et al. 2000), the minimum structure reconstruction (MSR) (Georgoulis & LaBonte 2006) which imposes $\mathbf{v}_\perp = 0$ as an assumption, or hybrid local-global methods such as inductive local correlation tracking (ILCT) (Welsch et al. 2004). These methods produce *a unique solution* for $\boldsymbol{\vartheta}$, but not necessarily *the unique solution* that corresponds to \mathbf{u} .

Several assumptions have been used either explicitly or implicitly to resolve the second ambiguity. Chae et al. (2001) conjecture that local correlation tracking (LCT) (Leese et al. 1970, 1971; November & Simon 1988) provides a direct estimate of the horizontal photospheric plasma velocity: $\boldsymbol{\vartheta}^{(\text{LCT})} = \mathbf{V}_h$. Démoulin & Berger (2003) conjecture that line-of-sight tracking methods, and in particular LCT, estimate the total flux transport velocity $\boldsymbol{\vartheta}^{(\text{LCT})} = \mathbf{U}$. Schuck (2005) formally demonstrated that LCT is consistent with the advection equation

$$\partial_t B_z + \boldsymbol{\vartheta}^{(\text{LCT})} \cdot \nabla_h B_z = 0, \quad (8)$$

not the continuity equation in (6), but that LCT could be modified to be consistent with (6) by direct integration along Lagrangian trajectories in an affine velocity profile. Nonetheless, both conjectures may be

considered in the context of (6). Under Chae et al.’s (2001) assumption, the flux transport velocity would be derived from line-of-sight optical flow methods via

$$\mathbf{u} B_z \equiv \boldsymbol{\vartheta} B_z - v_z \mathbf{B}_h, \quad (9)$$

where in principle, v_z might be approximately determined from Doppler velocities near disk center. Under Démoulin & Berger’s (2003) assumption, the total flux transport velocity would be derived from line-of-sight optical flow methods via

$$\mathbf{u} \equiv \boldsymbol{\vartheta} \text{ for } B_z \neq 0. \quad (10)$$

The *Ansatz* $\mathbf{u} = \boldsymbol{\vartheta}$ has important implications for solar observations. This conjecture implies that the total helicity and Poynting flux may be estimated by tracking the vertical magnetic field or by tracking the line-of-sight component near disk center as a proxy for the vertical magnetic field. Démoulin & Berger’s (2003) *Ansatz* has largely been accepted by the solar community (Welsch et al. 2004; Welsch et al. 2007; Kusano et al. 2004; Schuck 2005, 2006; LaBonte et al. 2007; Santos & Behner 2007; Tian & Alexander 2008; Zhang et al. 2008; Wang et al. 2008). However, equivalence between $\boldsymbol{\vartheta}$ and \mathbf{u} for line-of-sight methods has never been practically established. These two different hypotheses (9) and (10) for the interpretation of $\boldsymbol{\vartheta}$ inferred by DAVE will be considered in § 4.

The second ambiguity usually is not resolved using only information about the magnetic fields. The velocity field inferred by the IM (Kusano et al. 2002, 2004) does produce a component of the plasma velocity along the magnetic field, but this was simply subtracted off in Welsch et al. (2007). In the absence of a reference flow, possibly derived from Doppler measurements or LCT, the MEF imposes $v_{\parallel} = 0$ (Longcope 2004). ILCT and the original algebraic decomposition both assume $v_{\parallel} = 0$ (Welsch et al. 2004). Georgoulis & LaBonte (2006) describe a method for inferring v_{\parallel} from Doppler measurements for MSR. For DAVE4VM the second ambiguity is resolved simultaneously with the first. The DAVE4VM method estimates a *field aligned plasma velocity* from only magnetic field observations!

Using established computer vision techniques (Lucas & Kanade 1981; Lucas 1984; Baker & Matthews 2004), Schuck (2006) developed the DAVE from a short time-expansion of the modified LCT method discussed in Schuck (2005) for estimating velocities from line-of-sight magnetograms. The DAVE locally minimizes the square of the continuity equation (2b) subject to an affine velocity profile. Using “moving paint” experiments, Schuck (2006) demonstrated that this technique was faster and more accurate than existing LCT algorithms for data satisfying (2b). The DAVE method has been used to study the apparent motion of active regions (Schuck 2006), flux pile up in the photosphere (Litvinenko et al. 2007), and helicity flux in the photosphere (Chae 2007). However, nagging questions remain about its performance.

Welsch et al. (2007) set an important new standard for evaluating scientific optical flow methods used for studying the Sun. For the first time many existing methods for estimating photospheric velocities from magnetograms were tested on a reasonable approximation to synthetic photospheric data from anelastic pseudospectral ANMHD simulations (Fan et al. 1999; Abbett et al. 2000, 2004). The methods tested were Lockheed Martin’s Solar and Astrophysical Laboratory’s (LSAL) LCT code (DeRosa 2001), Fourier LCT (FLCT) (Welsch et al. 2004), the DAVE (Schuck 2006), the IM (Kusano et al. 2002, 2004), ILCT (Welsch et al. 2004), the MEF (Longcope 2004), and MSR (Georgoulis & LaBonte 2006). Unfortunately the results were not entirely encouraging. Welsch et al. (2007) treated the velocities estimated from line-of-sight methods as the flux transport velocities consistent with the hypothesis of Démoulin & Berger (2003) in (10). Evaluation of the DAVE’s performance on the ANMHD data under this assumption revealed that the DAVE method did not estimate the helicity flux or Poynting flux reliably. In fact none of the pure line-of-sight methods: LSAL’s LCT, FLCT, or the DAVE—estimated these fluxes reliably, reproducing (at best) respectively

11%, 9%, and 23% of the helicity rate, and reproducing respectively 6%, 11%, and 22% of the power injected through the surface.

Of course the ANMHD data have limitations. The simulation models the rise of a buoyant magnetic flux rope in the convection zone and represents the magnetic structure of granulation or super-granulation rather than the dynamics of an active region (See § 2 in Welsch et al. 2007, for a complete discussion). In addition, Welsch et al. (2007) noted that tracking methods performed better on real magnetograms than on the synthetic ANMHD data using “moving paint” experiments where images were simply shifted relative to one another. These results provoked them to comment “that the ANMHD data set either lacks some characteristic present in real solar magnetograms or contains artifacts not present in solar data.” Consequently, the poor performance of tracking methods on ANMHD data might be attributed to the de-aliasing method for nonlinear terms in ANMHD (truncating the spatial Fourier spectrum effectively smoothes small-scale structures) or perhaps to the Fourier ringing near strong fields in the ANMHD data set. While these issues are important to resolve, *they fail to fully explain the poor performance of the tracking methods to accurately reproduce the quantity they were designed to estimate, namely the helicity flux!*

This paper has two primary goals:

1. Develop a modified DAVE (Schuck 2006) that incorporates horizontal magnetic fields, termed the “differential affine velocity estimator for vector magnetograms” (DAVE4VM), and demonstrate its performance on the ANMHD simulation data. DAVE4VM performs much better than the original DAVE technique and roughly on par with the minimum energy fit (MEF) method developed by Longcope (2004) which was deemed to have performed the best overall in Welsch et al.’s (2007) comparison of velocity-inversion techniques.
2. Identify the reasons for the poor performance of DAVE in Welsch et al. (2007).

The paper attempts to follow, as closely as possible, the presentation of the DAVE in Schuck (2006) and the analysis of velocity inversion techniques by Welsch et al. (2007). For the remainder of this paper, lower case variables are used to represent the flux transport vector, flux transport velocity, plasma velocity, electric field, Poynting flux, and helicity flux estimates from the DAVE4VM and DAVE: \mathbf{f} , \mathbf{u} , \mathbf{v}_\perp , \mathbf{e}_\perp , s_z and h and the corresponding uppercase variables are used to represent the “ground truth” from ANMHD: \mathbf{F} , \mathbf{U} , \mathbf{V}_\perp , \mathbf{E}_\perp , S_z , and H . The one deviation from this notation involves $\boldsymbol{\vartheta}$ which denotes an optical flow estimate based on (6). Section (2) describes the DAVE4VM model and § 3 describes its application to the ANMHD data. For the most part, the plots and quantitative analysis presented in Welsch et al. (2007) are produced for the DAVE4VM and DAVE to facilitate inter-comparison and comparison to the other methods considered in Welsch et al. (2007). For the DAVE this analysis involves the explicit assumption that $\boldsymbol{\vartheta} = \mathbf{u}$. In § 4 the assumption $\boldsymbol{\vartheta} = \mathbf{u}$ for the DAVE is relaxed and compared with an alternative hypotheses that $\boldsymbol{\vartheta} = \mathbf{v}_h$ — that the DAVE produces a biased estimate of the total horizontal plasma velocity.

2. The DAVE4VM Model

The extension of the DAVE for horizontal magnetic fields is straight-forward. The plasma velocity is modeled with a three-dimensional affine velocity profile:

$$\mathbf{v}(\mathbf{P}; \mathbf{x}) = \begin{pmatrix} \hat{u}_0 \\ \hat{v}_0 \\ \hat{w}_0 \end{pmatrix} + \begin{pmatrix} \hat{u}_x & \hat{u}_y \\ \hat{v}_x & \hat{v}_y \\ \hat{w}_x & \hat{w}_y \end{pmatrix} \begin{pmatrix} x \\ y \end{pmatrix}, \quad (11)$$

where the hatted variables model the local plasma velocity profile. The coordinate system for the affine velocity profile is *not* aligned with the magnetic field. Therefore, the velocities are *not* guaranteed to be orthogonal to \mathbf{B} . However, the parallel (\parallel) and perpendicular (\perp) components of the plasma velocity may be determined from

$$v_{\parallel} = \frac{(\mathbf{v} \cdot \mathbf{B}) \mathbf{B}}{B^2}, \quad (12a)$$

$$\mathbf{v}_{\perp} = \mathbf{v} - \frac{(\mathbf{v} \cdot \mathbf{B}) \mathbf{B}}{B^2}, \quad (12b)$$

$$\mathbf{v}_{\perp h} = \mathbf{v}_h - \frac{(\mathbf{v} \cdot \mathbf{B}) \mathbf{B}_h}{B^2}, \quad (12c)$$

$$v_{\perp z} = v_z - \frac{(\mathbf{v} \cdot \mathbf{B}) B_z}{B^2}. \quad (12d)$$

The error metric

$$\mathcal{C}_{\text{SSD}} = \int dt dx^2 w(\mathbf{x} - \boldsymbol{\chi}, t - \tau) \{ \partial_t B_z(\mathbf{x}, t) + \nabla_h \cdot [B_z(\mathbf{x}, t) \mathbf{v}_h(\mathbf{P}, \mathbf{x} - \boldsymbol{\chi}) , \quad (13a)$$

$$-v_z(\mathbf{P}, \mathbf{x} - \boldsymbol{\chi}) \mathbf{B}_h(\mathbf{x}, t)] \}^2, \quad (13b)$$

$$= \boldsymbol{\eta} \cdot \langle \mathbf{S} \rangle \cdot \boldsymbol{\eta}$$

characterizes how well the local velocity profile satisfies the magnetic induction equation over a subregion of the magnetogram sequence defined by the window function $w(\mathbf{x} - \boldsymbol{\chi}, t - \tau)$ where $\mathbf{P} = (\hat{u}_0, \hat{v}_0, \hat{u}_x, \hat{v}_y, \hat{u}_y, \hat{v}_x, \hat{w}_0, \hat{w}_x, \hat{w}_y)$ is a vector of parameters and $\boldsymbol{\eta} \equiv (\mathbf{P}, 1)$. The plasma velocity $\mathbf{v}(\mathbf{P}, \mathbf{x} - \boldsymbol{\chi})$ in (13a) is referenced from the center of the window at $\mathbf{x} = \boldsymbol{\chi}$ so that \hat{u}_0 , \hat{v}_0 , and \hat{w}_0 represent the plasma velocities at the center of the window and the subscripted parameters represent the best fit local shears in the plasma flows, i.e. $\hat{u}_x = \partial_x (\hat{\mathbf{x}} \cdot \mathbf{v})$. The matrix elements of $\langle \mathbf{S} \rangle$ are defined by

$$\langle \mathbf{S} \rangle = \int dt dx^2 w(\mathbf{x} - \boldsymbol{\chi}, t - \tau) \mathbf{S}(\boldsymbol{\chi}; x, t), \quad (13c)$$

where

$$\mathbf{S}(\boldsymbol{\chi}; x, t) \equiv \begin{bmatrix} \mathbf{A} & \mathbf{b} \\ \mathbf{b} & \mathcal{G}_{99} \end{bmatrix} = \begin{bmatrix} \mathcal{G}_{00} & \cdot & \cdot & \cdot & \cdot & \cdot & \cdot & \cdot & \cdot & \cdot \\ \mathcal{G}_{10} & \mathcal{G}_{11} & \cdot & \cdot & \cdot & \cdot & \cdot & \cdot & \cdot & \cdot \\ \mathcal{G}_{20} & \mathcal{G}_{21} & \mathcal{G}_{22} & \cdot & \cdot & \cdot & \cdot & \cdot & \cdot & \cdot \\ \mathcal{G}_{30} & \mathcal{G}_{31} & \mathcal{G}_{32} & \mathcal{G}_{33} & \cdot & \cdot & \cdot & \cdot & \cdot & \cdot \\ \mathcal{G}_{40} & \mathcal{G}_{41} & \mathcal{G}_{42} & \mathcal{G}_{43} & \mathcal{G}_{44} & \cdot & \cdot & \cdot & \cdot & \cdot \\ \mathcal{G}_{50} & \mathcal{G}_{51} & \mathcal{G}_{52} & \mathcal{G}_{53} & \mathcal{G}_{54} & \mathcal{G}_{55} & \cdot & \cdot & \cdot & \cdot \\ \mathbf{s}_{60} & \mathbf{s}_{61} & \mathbf{s}_{62} & \mathbf{s}_{63} & \mathbf{s}_{64} & \mathbf{s}_{65} & \mathbf{s}_{66} & \cdot & \cdot & \cdot \\ \mathbf{s}_{70} & \mathbf{s}_{71} & \mathbf{s}_{72} & \mathbf{s}_{73} & \mathbf{s}_{74} & \mathbf{s}_{75} & \mathbf{s}_{76} & \mathbf{s}_{77} & \cdot & \cdot \\ \mathbf{s}_{80} & \mathbf{s}_{81} & \mathbf{s}_{82} & \mathbf{s}_{83} & \mathbf{s}_{84} & \mathbf{s}_{85} & \mathbf{s}_{86} & \mathbf{s}_{87} & \mathbf{s}_{88} & \cdot \\ \mathcal{G}_{90} & \mathcal{G}_{91} & \mathcal{G}_{92} & \mathcal{G}_{93} & \mathcal{G}_{94} & \mathcal{G}_{95} & \mathbf{s}_{96} & \mathbf{s}_{97} & \mathbf{s}_{98} & \mathcal{G}_{99} \end{bmatrix}, \quad (14)$$

is a real symmetric $\mathbf{S} = \mathbf{S}^*$ positive semidefinite structure tensor where a superscript “*” indicates the matrix transpose. The matrix elements of \mathbf{S} are provided in Appendix A. The elements \mathcal{G}_{ij} correspond to the original DAVE method (Schuck 2006) and the remainder \mathbf{s}_{ij} represent corrections due to the horizontal components of the magnetic field and flows normal to the surface. The least-squares solution is

$$\mathbf{P} = -\langle \mathbf{A} \rangle^{-1} \cdot \langle \mathbf{b} \rangle, \quad (15)$$

when the aperture problem is completely resolved $\det(\langle \mathbf{A} \rangle) \neq 0$ and the velocity field is unambiguous. However, there are important new terms in the structure tensor $\langle \mathbf{S} \rangle$ involving \mathbf{B}_h . Situations where $\det(\langle \mathbf{A} \rangle) = 0$ because $\mathbf{B}_h = 0$ or $B_z = 0$ over the region contained within the window must be considered. In general, the Moore-Penrose pseudo-inverse $\langle \mathbf{A} \rangle^\dagger$ provides a numerically stable estimate of the optical flow parameters even when $\det(\langle \mathbf{A} \rangle) = 0$

$$\mathbf{P} = -\langle \mathbf{A} \rangle^\dagger \cdot \langle \mathbf{b} \rangle, \quad (16a)$$

where

$$\langle \mathbf{A} \rangle^\dagger \equiv \mathbf{V} \mathbf{\Sigma}^\dagger \mathbf{U}^*, \quad (16b)$$

is defined in terms of the singular value decomposition (Golub & Van Loan 1980)

$$\langle \mathbf{A} \rangle = \mathbf{U} \mathbf{\Sigma} \mathbf{V}^*. \quad (16c)$$

Here \mathbf{U} and \mathbf{V} are orthonormal matrices corresponding to the nine principle directions, $\mathbf{\Sigma}$ is a diagonal matrix containing the nine singular values, and $\mathbf{\Sigma}^\dagger$ is computed by replacing *every nonzero element of $\mathbf{\Sigma}$* by its reciprocal. If $\mathbf{B}_h = 0$, the singular values along the vertical direction are zero and $\langle \mathbf{A} \rangle$ is rank deficient. In this case, the method implemented produces the minimum norm least squares solution resulting in no vertical flows: $w_0 = w_x = w_y = 0$.

3. Application to ANMHD Simulations

This paper considers the pair of vector magnetograms \mathbf{B} separated by the *shortest* time interval $\Delta t \approx 250$ s between data dumps of the ANMHD simulation slice archived by Welsch et al. (2007). The “ground truth” data are derived from the time-averaged velocity and magnetic fields from ANMHD over the *shortest* time interval. The region of interest in the ANMHD simulations corresponds to a 101×101 pixel region centered on a convection cell. Welsch et al. (2007) thresholded on the vertical magnetic field and considered only pixels with $|B_z| > 370$ G for all plots and quantities except for the total helicity where a different masking of results was used (Welsch et al. 2008). In a departure from the original presentation of Welsch et al. (2007) this paper considers pixels with $B = \sqrt{B_x^2 + B_y^2 + B_z^2} > 370$ G. This corresponds to 7013 pixels or roughly 70% of the region of interest. This difference in thresholding is important because most of the flux emergence and helicity flux in the simulation occurs along the neutral line in regions of weak vertical field that are missed with vertical field thresholding used in the original study. Note that the modified thresholding mask contains weak vertical field regions and contains substantially more points than the roughly 3800 used in Welsch et al. (2007). The difference between the helicity flux in this comparison region and the total simulation is 0.023%.

Since the DAVE4VM is a local optical flow method that determines the plasma velocities within a windowed subregion by constraining the local velocity profile, the choice of window size is a crucial issue for estimating velocities accurately. The window must be large enough to contain enough structure to uniquely determine the coefficients of the flow profile and resolve the aperture problem, but not so large as to violate the affine velocity profile (11) which is only valid locally (See Schuck 2006, for discussion of the aperture problem in the context of the DAVE). In Welsch et al. (2007), the optimal window size was chosen for the DAVE by examining the Pearson correlation and slope between $\nabla_h \cdot (\boldsymbol{\vartheta} B_z)$ and $\Delta B_z / \Delta t$ from ANMHD. If the method satisfies the induction equation exactly everywhere, the Pearson correlation and slope would both be equal to -1 . However both the DAVE and DAVE4VM were conceived with the recognition that real magnetograms contain noise and should not satisfy the magnetic induction equation exactly; these methods

satisfy the induction equation statistically within the window by minimizing the mean squared deviations from the ideal induction equations. Consequently, how well these methods satisfy the magnetic induction equation globally or over a subset of pixels can be used to assess overall performance. In Welsch et al. (2007), the DAVE was “optimized” over a subset of pixels with $|B_z| > 370$ G that did not include the weak vertical field regions discussed in this study. Using the Pearson correlation and slope, an asymmetric window of 21×39 performed the best on the ANMHD data. For the present study, the DAVE was “re-optimized” over the new criteria $|B| > 370$ G to provide an “apples-to-apples” comparison. However, I emphasize that generally this optimization cannot be carried out for the DAVE because this method was proposed for deriving flux-transport velocities from line-of-sight magnetograms. In this situation, the threshold mask can only be applied on the line-of-sight component *as a proxy* for the vertical magnetic field. Nonetheless, as a practical matter, understanding the accuracy limitation of the line-of-sight method in comparison to the vector method when synthetic vector magnetograms are available will reveal the relative reliability of helicity flux studies that used optical flow methods that rely exclusively on the line-of-sight magnetic field under the “best case scenario” for the tracking methods: the true vertical magnetic field is tracked and regions that contain interesting physics are known *a-priori*. By using the “ground truth” vertical magnetic field, the evaluation is biased to *favor* the performance of the DAVE method over what would be possible under realistic conditions where only the line-of-sight magnetic field is available.

Five different criteria were used to optimize window selection. Only symmetric windows were considered and some improvement in the results can be achieved by implementing asymmetric windows as in Welsch et al. (2007). Figure 1 shows the optimization curves for the DAVE (*left*) and DAVE4VM (*right*). The top plots show the Spearman rank order (ρ ; *dashed black*) and Pearson (C ; *solid black curve*) correlations and slope (S ; *red curve*) between $\nabla_h \cdot (\boldsymbol{\vartheta} B_z)$ and $\Delta B_z / \Delta t$ for DAVE and $\nabla_h \cdot (\mathbf{u} B_z)$ and $\Delta B_z / \Delta t$ for DAVE4VM using pixels that satisfy $|B| > 370$ G. The gradients were computed with 5-point least-squares optimized derivatives (Jähne 2004). Window sizes between 15 and 30 pixels provide the best balance for achieving performance approaching $C = \rho = S = -1$. Increasing the window size beyond 30 pixels continues to improve the Spearman and Pearson correlations but with diminishing returns while the slopes degrade significantly. The bottom plots show the power (*black curve*) and helicity rate (*red curve*) as a function of window size for the DAVE and DAVE4VM. For DAVE these calculations require the assumption that $\boldsymbol{\vartheta} = \mathbf{u}$. The horizontal black and red dashed lines correspond to the ground truth Poynting and helicity flux from ANMHD. The magnitude of these fluxes are maximum near 20 pixels with roughly uniform performance between 15 and 30 pixels. A window size¹ of 23 pixels was chosen for both the DAVE and DAVE4VM as indicated by the vertical dot-dashed lines in Figure 1. These objective metrics for evaluation of global performance can be implemented without knowledge of ground truth. Only future tests with more realizations of synthetic data can reveal whether they are robust metrics for optimizing window choice. Table 1 presents a summary of the correlation coefficients on the mask $|B| > 370$ G characterizing the accuracy of the DAVE and DAVE4VM for the quantities discussed in this section.

3.1. Flux Transport Vectors and Plasma Velocities

Determining the flux transport vectors $\mathbf{f} = \mathbf{u} B_z$ is equivalent to determining the perpendicular plasma velocities \mathbf{v}_\perp . The accuracy of the flux transport vectors is critical for estimating other MHD quantities:

¹Only windows with odd numbers of pixels on each side of the window are possible in these implementations of the DAVE and DAVE4VM.

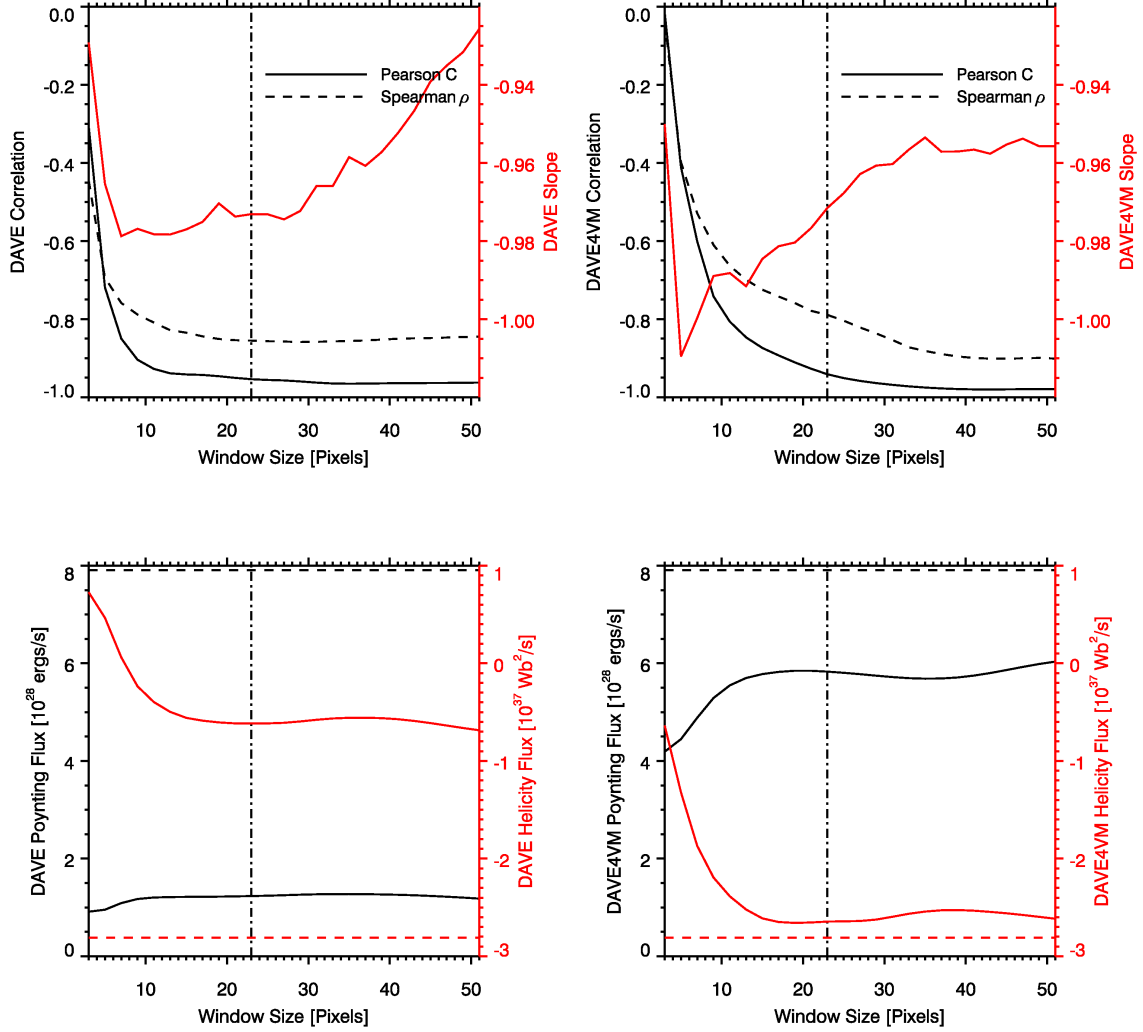


Fig. 1.— Optimization curves for the DAVE (*left*) and DAVE4VM (*right*). (top) The Spearman rank order (*dashed black curve*) and Pearson (*solid black curve*) correlations and slope (*red curve*) between $\nabla_h \cdot (\boldsymbol{\vartheta} B_z)$ and $\Delta B_z / \Delta t$ for DAVE and $\nabla_h \cdot (\boldsymbol{u} B_z)$ and $\Delta B_z / \Delta t$ for DAVE4VM as a function of window size. (bottom) The power (black) and helicity (red) as a function of window size; this assumes $\boldsymbol{\vartheta} = \boldsymbol{u}$ for DAVE. The horizontal black and red dashed lines correspond to the ground truth power and helicity rate through the simulation slice from ANMHD. The vertical dot-dashed lines indicate the “optimal” window size of 23 pixels chosen for both DAVE and DAVE4VM.

Table 1. Comparison between the DAVE and DAVE4VM over the 7013 pixels that satisfy $|\mathbf{B}| > 370$ G in Figure 2. This mask contain regions of weak vertical field not considered in Welsch et al. (2007).

Quantities		DAVE (Assuming $\boldsymbol{\vartheta} = \mathbf{u}$)			DAVE4VM		
		Spearman	Pearson	Slope	Spearman	Pearson	Slope
$u_x B_z$	$U_x B_z$	0.34	0.57	0.15	0.88	0.89	0.80
$u_y B_z$	$U_y B_z$	0.70	0.76	0.71	0.94	0.90	0.89
$v_{\perp x}$	$V_{\perp x}$	0.87	0.85	0.91	0.89	0.88	0.94
$v_{\perp y}$	$V_{\perp y}$	0.93	0.92	1.20	0.94	0.94	1.00
$v_{\perp z}$	$V_{\perp z}$	0.17	0.28	0.07	0.80	0.80	0.79
$\nabla_h \cdot (\mathbf{u} B_z)$	$\Delta B_z / \Delta t$	-0.85	-0.95	-0.97	-0.79	-0.94	-0.97
$e_{\perp x}$	$E_{\perp x}$	0.70	0.76	0.71	0.94	0.90	0.89
$e_{\perp y}$	$E_{\perp y}$	0.34	0.57	0.15	0.88	0.89	0.80
$e_{\perp z}$	$E_{\perp z}$	0.96	0.96	1.20	0.94	0.97	1.00
s_z	S_z	0.20	0.12	0.04	0.88	0.83	0.71

Table 2. Comparison of accuracy of the velocity estimates between the DAVE and DAVE4VM over the 7013 pixels that satisfy $|\mathbf{B}| > 370$ G in Figure 2. This mask contains regions of weak vertical field not considered in Welsch et al. (2007). Here $\langle |\delta \tilde{\mathbf{f}}| \rangle$ is the average fractional error, $\langle \delta |\tilde{\mathbf{f}}| \rangle$ is the average error in magnitude, C_{vec} is the vector correlation, C_{CS} is the direction correlation, and $\langle \cos \theta \rangle_W$ is weighted direction cosine.

\mathbf{f}	DAVE (Assuming $\boldsymbol{\vartheta} = \mathbf{u}$)					DAVE4VM				
	$\langle \delta \tilde{\mathbf{f}} \rangle$	$\langle \delta \tilde{\mathbf{f}} \rangle$	C_{vec}	C_{CS}	$\langle \cos \theta \rangle_W$	$\langle \delta \tilde{\mathbf{f}} \rangle$	$\langle \delta \tilde{\mathbf{f}} \rangle$	C_{vec}	C_{CS}	$\langle \cos \theta \rangle_W$
$\mathbf{u} B_z$	0.83 ± 0.25	-0.47 ± 0.34	0.61	0.52	0.71	0.38 ± 0.26	-0.09 ± 0.21	0.91	0.92	0.95
\mathbf{v}_{\perp}	0.72 ± 0.30	0.09 ± 0.27	0.81	0.77	0.87	0.40 ± 0.25	0.01 ± 0.14	0.93	0.90	0.92

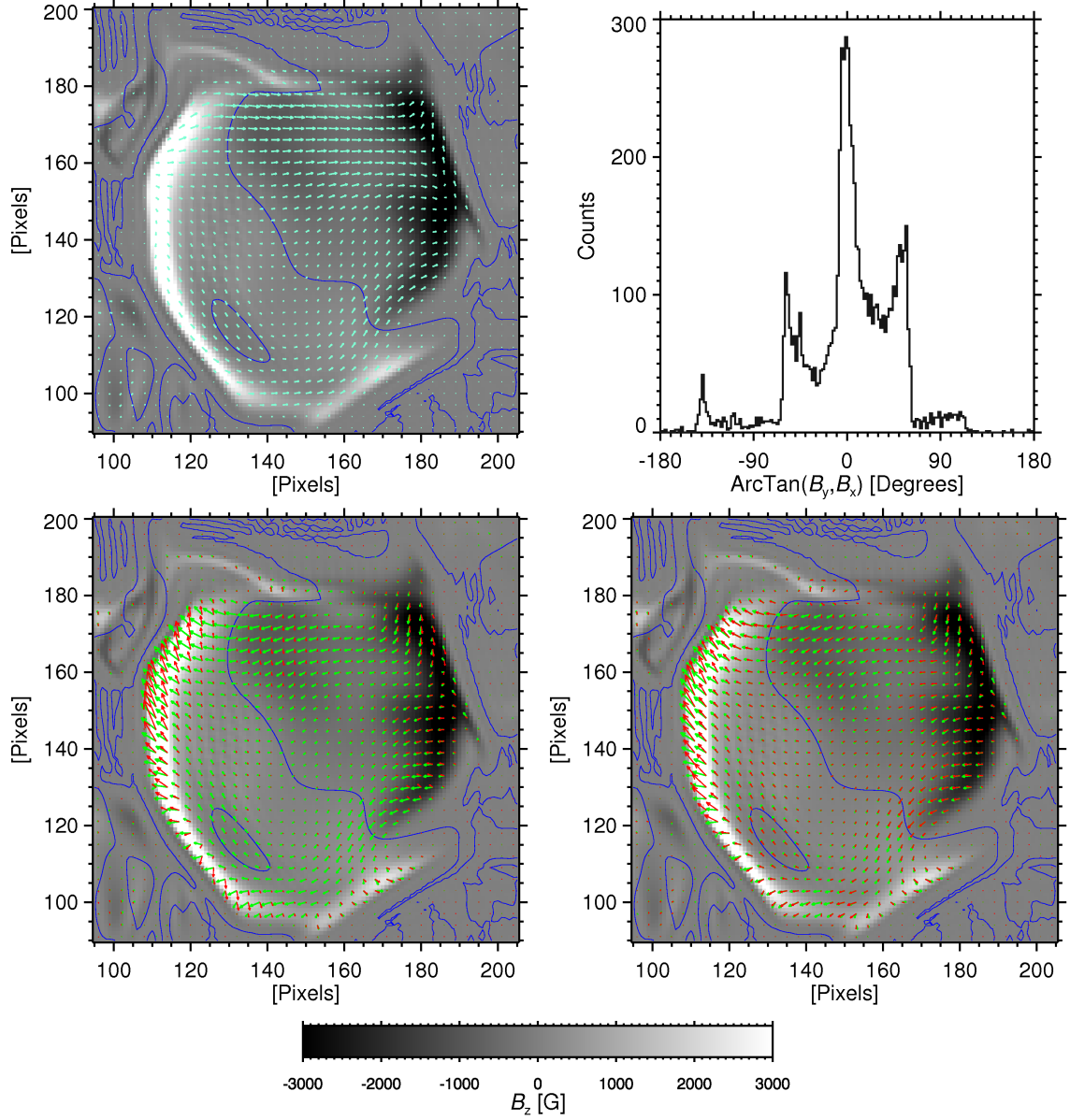


Fig. 2.— Top left: Grey scale image of the vertical magnetic field B_z overlaid with the horizontal magnetic field vectors \mathbf{B}_h in aqua. Blue contours indicate smoothed neutral lines. Top right: Distribution of angles for \mathbf{B}_h in the horizontal plane. Bottom: (red arrows) $\boldsymbol{\vartheta} B_z$ for the DAVE (*left*) and $\mathbf{u} B_z$ for the DAVE4VM (*right*) plotted over ANMHD’s flux transport vectors $\mathbf{U} B_z$ (green arrows). Vectors are shown only for pixels in which $|B| > 370$ G, and for clarity, only every third vector is displayed.

perpendicular plasma velocities, electric field, helicity flux, Poynting flux, etc, since all of these quantities may be derived directly from flux transport vectors.

3.1.1. Flux Transport Velocities and Perpendicular Plasma Velocities

The top left of Figure 2 shows the region of interest from the ANMHD simulations with grey scale image of vertical magnetic field overlaid with the horizontal magnetic field vectors \mathbf{B}_h in aqua. The blue contours indicate smoothed neutral lines. The top right shows the distribution of angles for \mathbf{B}_h in the horizontal plane. The horizontal magnetic field is largely aligned with the $\hat{\mathbf{x}}$ -axis as indicated by the aqua vectors in the left panel and the strong peak in the histogram near $\arctan(B_y, B_x) \approx 0^\circ$ in the right panel.² There is also significant alignment of the magnetic field with $\pm 60^\circ$ and alignment of weak fields with -140° . The bottom panels show $\boldsymbol{\vartheta} B_z$ from DAVE (*left*) and $\mathbf{u} B_z$ from DAVE4VM in red (*right*) and the flux transport vectors $\mathbf{F} = \mathbf{U} B_z$ from ANMHD in green. The improvement between the DAVE and DAVE4VM is manifest — finding a region where the DAVE4VM performs qualitatively worse than the DAVE is difficult. The DAVE4VM performs the worst in the region $140 - 160 \times 150 - 170$ where the flux transport vectors run roughly anti-parallel to the horizontal magnetic field and there is little structure in the vertical component.

Figure 3 shows scatter plots of the $\boldsymbol{\vartheta} B_z$ from DAVE (*left*) and $\mathbf{u} B_z$ from DAVE4VM (*right*) versus the flux transport vectors $\mathbf{U} B_z$ from ANMHD. Red and blue are used to distinguish x - and y -components, respectively. The nonparametric Spearman rank-order correlation coefficients (ρ), Pearson correlation coefficients (C), and slopes (S) estimated by the least absolute deviation method are shown for both components of the flux transport vectors. Both visually and quantitatively the DAVE4VM’s correlation with ANMHD is much higher than the DAVE’s. The correlation coefficients even match or exceed the correlation coefficients for the flux transport vectors from the DAVE and MEF reported for the restricted mask $|B_z| > 370$ G in Welsch et al. (2007). In particular, DAVE does not accurately estimate the flux transport vectors in the $\hat{\mathbf{x}}$ -direction. The correlation coefficients for this $\hat{\mathbf{x}}$ -component of the flux transport vectors are $\rho_x = 0.34$ and $C_x = 0.57$ with a slope of $S_x = 0.15$. Since that the $\hat{\mathbf{x}}$ -direction is the predominant direction of the horizontal magnetic for the ANMHD data, the low correlation coefficients suggest that DAVE is insensitive to flux emergence which is proportional to $v_z \mathbf{B}_h$. This will be discussed further in § 4.

Figure 4 shows scatter plots of the estimated perpendicular plasma velocities \mathbf{v}_\perp from the DAVE assuming $\boldsymbol{\vartheta} = \mathbf{u}$ (*left*) and DAVE4VM (*right*) versus ANMHD’s perpendicular plasma velocities \mathbf{V}_\perp . Red, blue, and black correspond to the x -, y -, and z -components respectively. The nonparametric Spearman rank-order correlation coefficients (ρ), Pearson correlation coefficients (C), and slopes (S) estimated by the least absolute deviation method are shown for each component of the perpendicular plasma velocities. The DAVE4VM’s correlation coefficients match or exceed the correlation coefficients for the perpendicular plasma velocities from the DAVE. Particularly striking is the DAVE4VM’s relatively higher correlation for the perpendicular vertical plasma velocity $\mathbf{v}_{\perp z}$ which *exceeds* the correlation for the DAVE by roughly $0.5 - 0.6$. The improvement in the DAVE4VM’s estimate is due to the *explicit* inclusion of horizontal magnetic fields and vertical flows. The flux transport and perpendicular plasma velocity estimates are further quantified by considering the metrics used by Schrijver et al. (2006), Welsch et al. (2007), and Metcalf et al. (2008). The

² $\arctan(y, x) \equiv \arctan(y/x)$.

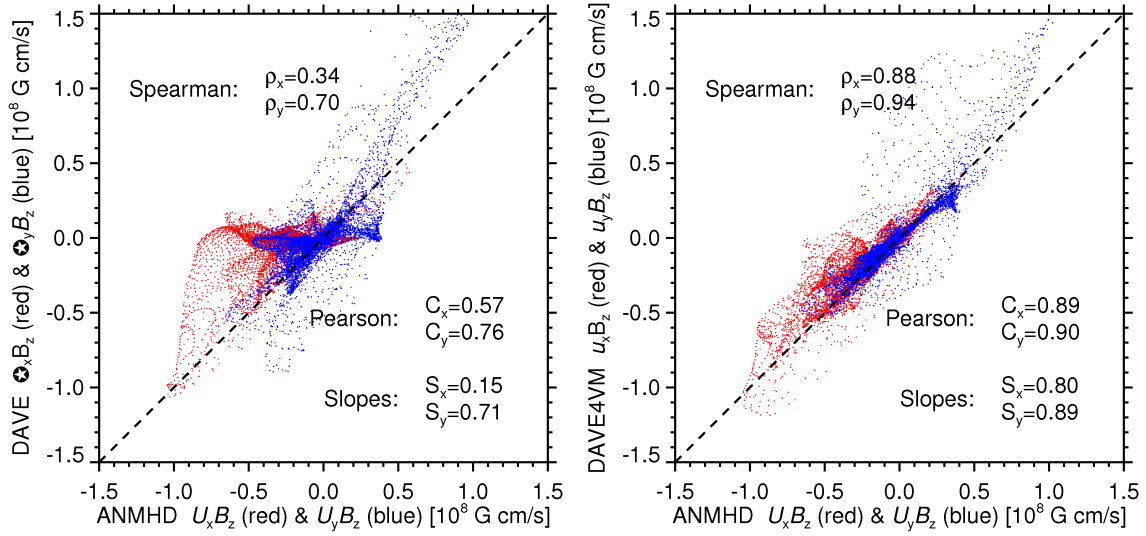


Fig. 3.— Scatter plots of ϑB_z for the DAVE (*left*) and $\mathbf{u} B_z$ for the DAVE4VM (*right*) versus ANMHD’s flux transport vectors, $\mathbf{F} = \mathbf{U} B_z$. Red and blue are used to distinguish x - and y -components, respectively. The nonparametric Spearman rank-order correlation coefficients (ρ), Pearson correlation coefficients (C), and slopes (S) estimated by the least absolute deviation method are shown for both components of the flux transport vectors.

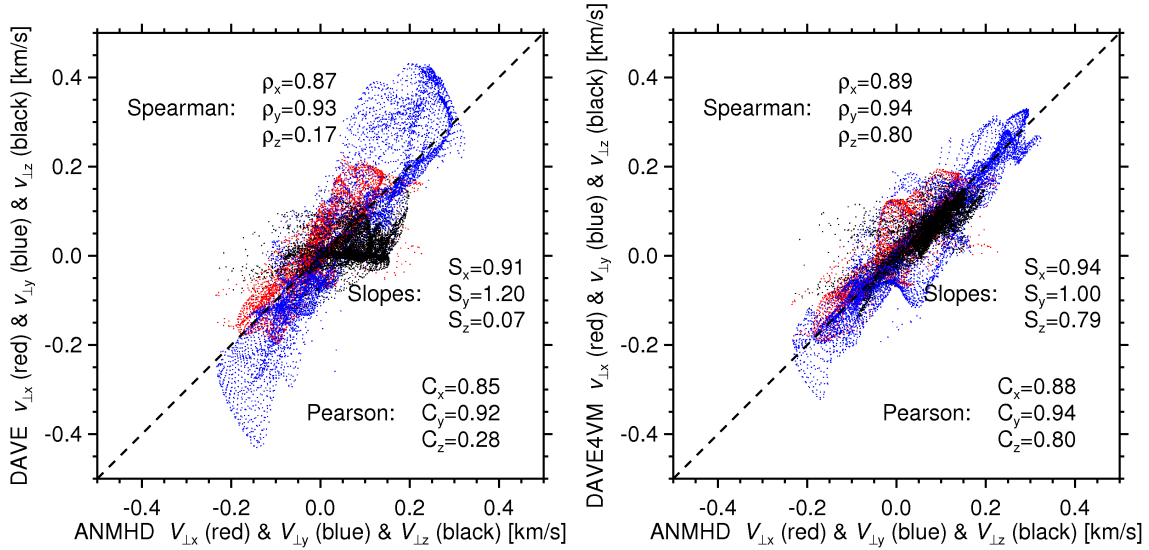


Fig. 4.— Scatter plots of the estimated perpendicular plasma velocities \mathbf{v}_\perp from DAVE assuming $\vartheta = \mathbf{u}$ (*left*) and DAVE4VM (*right*) versus the perpendicular plasma velocities \mathbf{V}_\perp from ANMHD. Red, blue, and black correspond to the x -, y - and z -components respectively. The nonparametric Spearman rank-order correlation coefficients (ρ), Pearson correlation coefficients (C), and slopes (S) are shown for each component of the perpendicular plasma velocities.

fractional error between the estimated vector \mathbf{f} and the true vector \mathbf{F} at the i th pixel is

$$|\delta \tilde{\mathbf{f}}_i| \equiv \frac{|\mathbf{f}_i - \mathbf{F}_i|}{|\mathbf{F}_i|}, \quad (17a)$$

whereas the fractional error in magnitude is

$$\delta |\tilde{\mathbf{f}}_i| \equiv \frac{|\mathbf{f}_i| - |\mathbf{F}_i|}{|\mathbf{F}_i|}. \quad (17b)$$

The moments of these error metrics or any quantity q may be accumulated over the N pixels within the masks (either $|\mathbf{B}| > 370$ G or $|B_z| > 370$ G) producing the average

$$\langle q \rangle \equiv \frac{1}{N} \sum_{i=1}^N q_i, \quad (18a)$$

and the variance

$$\sigma_q^2 \equiv \frac{1}{N-1} \sum_{i=1}^N (q_i - \langle q \rangle)^2. \quad (18b)$$

For perfect agreement between the estimates and the “ground truth” from ANMHD, $\langle |\delta \tilde{\mathbf{f}}| \rangle$, $\langle \delta |\tilde{\mathbf{f}}| \rangle$, and their associated variances would be zero. Two measures of directional error are considered, the vector correlation

$$C_{\text{vec}} = \frac{\langle \mathbf{f} \cdot \mathbf{F} \rangle}{\sqrt{\langle \mathbf{f}^2 \rangle \langle \mathbf{F}^2 \rangle}}, \quad (19a)$$

and the direction correlation

$$C_{\text{CS}} = \left\langle \frac{\mathbf{f} \cdot \mathbf{F}}{\sqrt{\mathbf{f}^2 \mathbf{F}^2}} \right\rangle \equiv \langle \cos \theta \rangle. \quad (19b)$$

Both metrics range from -1 for antiparallel vector fields, to 0 for orthogonal vector fields, and to 1 for parallel vector fields (perfect agreement). Table 2 shows these metrics for the DAVE and DAVE4VM over the mask $|\mathbf{B}| > 370$ G. The DAVE4VM has fractional errors less than or equal to 0.4 whereas the fractional errors for the DAVE exceed 0.7 for both the flux transport vectors and the perpendicular plasma velocities. The average bias error in the magnitude is improved for the DAVE4VM over the DAVE. For the flux transport vectors the bias error in magnitude is -0.09 and -0.47 for DAVE4VM and DAVE respectively which corresponds to a factor of 5 improvement. For the plasma velocity, the bias error in magnitude is 0.01 and 0.09 for DAVE4VM and DAVE respectively which corresponds to a factor of 9 improvement. The vector correlation is larger for DAVE4VM than for DAVE. For DAVE4VM $C_{\text{vec}} \gtrsim 0.9$ for both the flux transport velocity and the perpendicular plasma velocities. In contrast, for the DAVE there is a substantial difference in the accuracy of the flux transport vectors with $C_{\text{vec}} = 0.61$ and the perpendicular plasma velocities with $C_{\text{vec}} = 0.81$. Finally the directional errors are smaller for the DAVE4VM than for the DAVE. For the DAVE4VM $C_{\text{CS}} \gtrsim 0.9$ for both the flux transport vectors and the perpendicular plasma velocities. Again, for the DAVE there is a substantial difference in the accuracy of the flux transport vectors with $C_{\text{CS}} = 0.52$ and the perpendicular plasma velocities with $C_{\text{CS}} = 0.77$.

The direction correlation C_{CS} is difficult to translate into average angular error because it is a nonlinear function of θ and does not indicate whether the estimated vectors “lead” or “lag” the “ground truth” on average. For the 2D flux transport vectors the moments of the distribution of angular errors

$$\theta = \arctan[(\mathbf{u} \times \mathbf{U})_z, \mathbf{u} \cdot \mathbf{U}], \quad (20)$$

can be more informative. Figure 5 shows histograms of the angles between $\mathbf{u} B_z$ and $\mathbf{U} B_z$ for the DAVE (*left*) and DAVE4VM (*right*). This is a quantitative estimate of the errors in directions of the flux transport vectors. The DAVE4VM represents a dramatic improvement over the DAVE. The DAVE4VM produces a nearly unimodal distribution peaked near 0° , whereas the DAVE produces a multi-peaked distribution with the largest peak at 80° and a variance that is more than twice as large as DAVE4VM.

Metrics such as (17) and (19) weight all estimates equally. To address this Metcalf et al. (2008) suggested weighting the errors. For example, the weighted direction cosine between an inferred vector and the ground truth vector may be defined as

$$\langle \cos \theta \rangle_W \equiv \frac{\langle W \cos \theta \rangle}{\langle W \rangle} \quad (21)$$

where W represents weights. For the flux transport velocity, the errors in the orientation of \mathbf{u} are more important where $|\mathbf{U} B_z|$ is large and less important where $|\mathbf{U} B_z|$ is small which suggests a weighting factor $W_i = |(\mathbf{U} B_z)|$. For perfect agreement $\langle \cos \theta \rangle_W = 1$. The weighted direction cosines for the flux transport vectors and the plasma velocities are reported in Table 2. Comparing the values of C_{CS} and $\langle \cos \theta \rangle_W$ demonstrates that weighting the direction cosine improves the apparent performance of DAVE but the results for DAVE4VM are essentially unchanged. This suggests that DAVE4VM estimates velocities better than DAVE in regions of weak flux transport.

3.1.2. Parallel Velocity

Under ideal conditions, the magnetic field is only affected by $\nabla \times (\mathbf{v} \times \mathbf{B})$. Consequently, only the inductive potential ϕ in (7) may be uniquely determined from the evolution of \mathbf{B} alone. The electrostatic potential ψ must *and can* be estimated with additional judicious assumptions. These additional assumptions correspond to the minimum photospheric velocity consistent with (7) for the global method MEF and to the prescribed affine form of the local plasma velocity for the local method DAVE4VM. The constraint of the affine velocity profile permits DAVE4VM to determine the electrostatic potential ψ from the *nonlocal* structure of the inductive potential ϕ . DAVE4VM uses unambiguous “pieces” of the plasma velocity within the window aperture to reconstruct the total plasma velocity at the center of the aperture. Within the notation of the Helmholtz decomposition, DAVE4VM estimates the local electrostatic field from the structure of the nonlocal inductive field within the aperture window by imposing a smoothness constraint on the velocity (the affine velocity profile). The accuracy of this estimate for the electrostatic field depends on the validity of the local affine velocity profile and the amount of structure in the local magnetic field; local methods cannot detect motion in regions of uniform magnetic field.

While researchers have widely recognized that estimating the electrostatic potential ψ from (5a) requires additional assumptions, they have not generally recognized that the parallel velocity v_{\parallel} may be estimated by the analogous arguments. In the absence of a reference flow, the MEF constrains the velocity to be perpendicular to the magnetic field: $v_{\parallel} = 0$. In contrast to the velocity estimated by DAVE4VM is not constrained to be perpendicular to the local magnetic field. Instead, DAVE4VM fits an affine velocity model to the magnetic induction equation in an aperture window. This affine velocity model couples the dynamics across pixels within the window aperture. If there is sufficient structuring in the direction of the magnetic field within the aperture, i.e., the perpendicular plasma velocity points in different directions at different pixels within the aperture, then DAVE4VM can resolve the ambiguity in the field-aligned component of the plasma velocity at the center of the aperture.

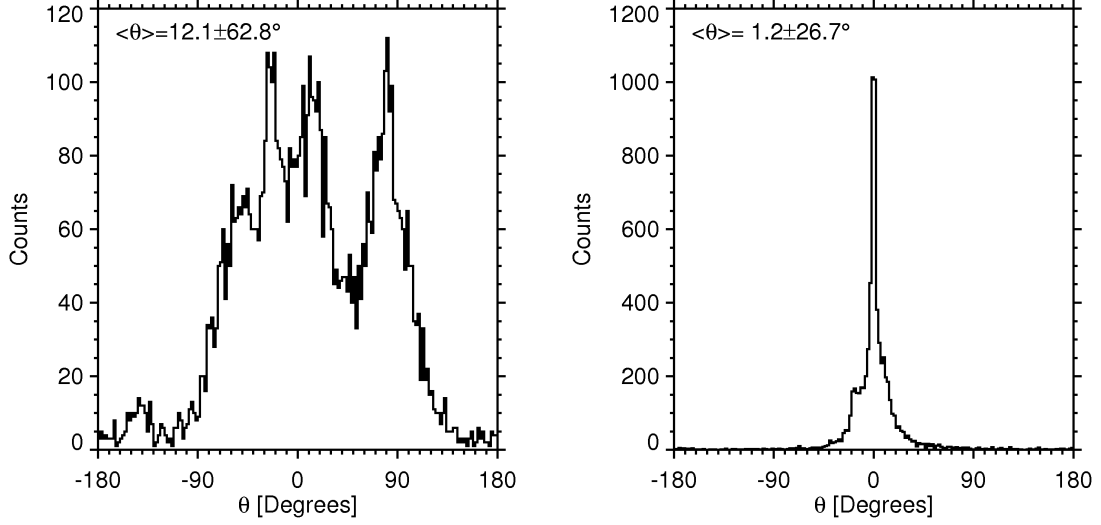


Fig. 5.— Histograms of the angles between ϑB_z and $U B_z$ for the DAVE (*left*) and between $u B_z$ and $U B_z$ for the DAVE4VM (*right*). The mean (bias) and standard deviation are reported in the upper left-hand corners.

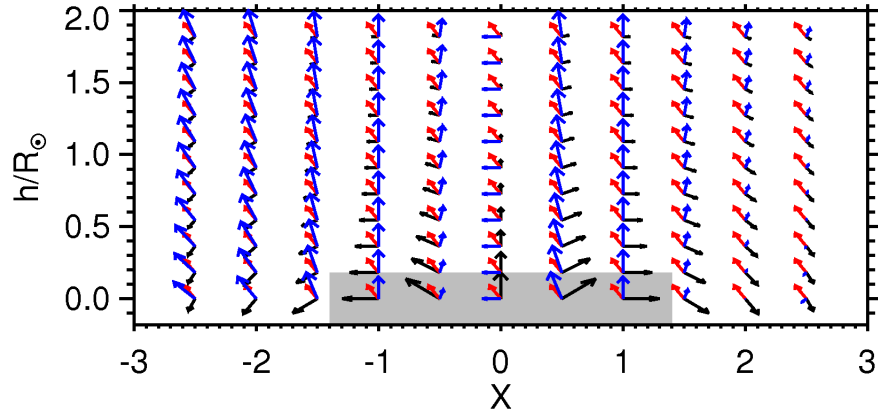


Fig. 6.— Schematic diagram of a uniform plasma flow across a diverging magnetic field above the photosphere at $h = 0$. The black arrows indicate the strength and direction of the magnetic field, the red arrows indicate the direction of the spatially uniform total plasma velocity \mathbf{v} , and the blue arrows indicate the magnitude and direction of the perpendicular plasma velocity \mathbf{v}_\perp . The aperture in the photosphere is indicated by the gray box.

Consider the simplified two-dimensional situation illustrated by the schematic diagram in Figure 6 of spatially uniform plasma flow across a diverging magnetic field above the photosphere at $h = 0$. The black arrows indicate the magnitude and direction of the magnetic field, the red arrows indicate the direction of the spatially uniform total plasma velocity \mathbf{v} , and the blue arrows indicate the magnitude and direction of the perpendicular plasma velocity \mathbf{v}_\perp . The aperture in the photosphere is indicated by the gray box. Within the aperture, the perpendicular plasma velocity captures a different component of the total plasma velocity at different locations; this is a consequence of the structuring of the magnetic field. Under the smoothness assumption of a uniform velocity profile, the velocity along the magnetic field in the $\hat{\mathbf{z}}$ -direction at $x = 0$ may be determined from the components of the perpendicular plasma velocity in the $\hat{\mathbf{z}}$ direction *at other locations within the aperture*. Using the N pixels in the window aperture results in an overdetermined system for the *total plasma velocity*:

$$\underbrace{\begin{bmatrix} \frac{B_z^2(\mathbf{x}_1)}{B^2(\mathbf{x}_1)} & -\frac{B_x(\mathbf{x}_1)B_z(\mathbf{x}_1)}{B^2(\mathbf{x}_1)} \\ -\frac{B_x(\mathbf{x}_1)B_z(\mathbf{x}_1)}{B^2(\mathbf{x}_1)} & \frac{B_x^2(\mathbf{x}_1)}{B^2(\mathbf{x}_1)} \\ \vdots & \vdots \\ \frac{B_z^2(\mathbf{x}_N)}{B^2(\mathbf{x}_N)} & -\frac{B_x(\mathbf{x}_N)B_z(\mathbf{x}_N)}{B^2(\mathbf{x}_N)} \\ -\frac{B_x(\mathbf{x}_N)B_z(\mathbf{x}_N)}{B^2(\mathbf{x}_N)} & \frac{B_x^2(\mathbf{x}_N)}{B^2(\mathbf{x}_N)} \end{bmatrix}}_{\mathbf{D}} \begin{pmatrix} v_x \\ v_z \end{pmatrix} = \underbrace{\begin{bmatrix} v_{\perp x}(\mathbf{x}_1) \\ v_{\perp z}(\mathbf{x}_1) \\ \vdots \\ v_{\perp x}(\mathbf{x}_N) \\ v_{\perp z}(\mathbf{x}_N) \end{bmatrix}}_{\mathbf{d}}, \quad (22a)$$

which has the solution (Golub & Van Loan 1980)

$$\begin{pmatrix} \hat{v}_x \\ \hat{v}_z \end{pmatrix} = (\mathbf{D}^* \mathbf{D})^{-1} \mathbf{D}^* \mathbf{d}. \quad (22b)$$

Note that $\mathbf{D}^* \mathbf{D}$ is analogous to $\langle \mathbf{A} \rangle$ and $\mathbf{D}^* \mathbf{d}$ is analogous to $\langle \mathbf{b} \rangle$ in (15).

This pedagogical example illustrates how DAVE4VM may analogously estimate the field-aligned plasma velocity for the more general case of a spatially variable plasma flow in an inhomogeneous magnetic field for (15). The accuracy of the estimate of the parallel velocity will be limited by the structuring in direction of the magnetic field within the aperture; if the magnetic field has a uniform orientation in the aperture window, no useful estimate of the field-aligned plasma velocity can be made from the magnetic measurements alone. The quality of the estimate may be assessed with the conditioning of $\mathbf{D}^* \mathbf{D}$ in (22b) for the pedagogical example or $\langle \mathbf{A} \rangle$ in (15) for the full system.

Figure (7) shows scatter plots of (*left*) the estimated parallel plasma velocities v_\parallel from DAVE4VM versus the parallel plasma velocities V_\parallel from ANMHD and (*right*) the estimated *total* plasma velocity \mathbf{v} from DAVE4VM versus the *total* plasma velocities \mathbf{V} from ANMHD. The nonparametric Spearman rank-order correlation coefficients (ρ), Pearson correlation coefficients (C), and slopes (S) estimated by the least absolute deviation method are shown. The comma-separated pairs of numbers in the right plot, corresponding to correlations between \mathbf{v} and \mathbf{V} and \mathbf{v}_\perp and \mathbf{V} respectively, represent the relative improvement in total velocity estimate over the simple null hypothesis $H_0 : \mathbf{v} = \mathbf{v}_\perp$ that the total plasma velocity is the perpendicular plasma velocity. The correlation of the $\hat{\mathbf{x}}$ -component of total velocity is significantly improved over the null hypothesis H_0 . This improvement is interesting since the horizontal magnetic field is predominantly aligned with the \mathbf{x} -axis (See Figure 2). The correlation of the $\hat{\mathbf{y}}$ -component of total velocity is slightly worse than the null hypothesis. Finally, the correlation of the $\hat{\mathbf{z}}$ -component of total velocity is mixed with the Spearman correlation ρ slightly worse than the null hypothesis and the Pearson correlation C slightly better than the null hypothesis. However, the slopes of all three components are improved over the null hypothesis.

The significance of the correlations in the left plot may be tested against the null hypothesis $H_0 : \rho = 0$ by the Fisher permutation test. Fieller et al. (1957) have demonstrated with analysis backed Monte-Carlo simulation that Fisher’s z -transform of the correlation coefficient

$$z_S(\rho) = \frac{1}{2} \log \left| \frac{1+\rho}{1-\rho} \right|, \quad (23)$$

produces approximately normally distributed values. For example, permuting the values of v_{\parallel} and V_{\parallel} 10,000 times generates the null hypothesis distribution with $\langle z_S \rangle = 0.00 \pm 0.01$. The Spearman correlation coefficient $\rho = 0.53$ has a z -transform of $z_S(0.53) = 0.60$ which is roughly 50 standard deviations from the mean of the null distribution indicating that the parallel velocity correlation is statistically significant and not due to sampling error. However, the correlation $\rho = 0.53$ is small and the parallel velocity estimates may not be scientifically significant for accurately predicting the parallel velocity. The plasma velocities may be further constrained by introducing Doppler velocities, but this is beyond the scope of the present discussion.

3.1.3. Are \mathbf{v}_h and v_z Redundant?

DAVE4VM has incorporated an additional component of the velocity over DAVE by introducing three additional variables \hat{w}_0 , \hat{w}_x and \hat{w}_y . Consequently, one may reasonably wonder “are the terms $\mathbf{v}_h B_z$ and $v_z \mathbf{B}_h$ redundant for DAVE4VM?” The answer is a clear “No” for the ANMHD data. Equation (2a) is composed of two terms $B_z \mathbf{V}_h$ and $V_z \mathbf{B}_h$ describing shearing motion and emergence respectively. Figure 8 shows scatterplots of the two terms for the $\hat{\mathbf{x}}$ (*left*) and $\hat{\mathbf{y}}$ (*right*) components of (2a). The scatterplots indicate the *lack* of correlation between the terms describing shearing motions $B_z \mathbf{V}_h$ and emergence $V_z \mathbf{B}_h$. Red points indicate the results for DAVE4VM and blue points indicate the results for ANMHD. The Spearman rank order (ρ) and Pearson (C) correlations between the two terms, summarized in Table 3, are very low for both components of the flux transport velocities from DAVE4VM or ANMHD. These terms describe different physics, that are uncorrelated, and which require independent variables to describe.

3.2. Induction Equation and Electric Fields

Figure 9 shows $\nabla_h \cdot (\boldsymbol{\vartheta} B_z)$ from the DAVE (*left*) and $\nabla_h \cdot (\mathbf{u} B_z)$ from DAVE4VM (*right*) versus $\Delta B_z / \Delta t$ from ANMHD. The derivatives for these plots were estimated from 5-point optimized least squares. These plots indicate how well the two methods satisfy the MHD induction equation globally. The DAVE has higher

Table 3. The Spearman rank order (ρ) and Pearson (C) correlations between the terms in the flux transport velocity describing shearing motion and flux emergence.

Correlates		DAVE4VM		ANMHD	
		Spearman	Pearson	Spearman	Pearson
$v_{\perp x} B_z$	$v_{\perp z} B_x$	-0.23	-0.08	-0.12	-0.01
$v_{\perp y} B_z$	$v_{\perp z} B_y$	-0.07	-0.11	-0.09	-0.02
$v_{\perp x}$	$v_{\perp z}$	-0.09	-0.10	-0.15	-0.15
$v_{\perp y}$	$v_{\perp z}$	-0.34	-0.33	-0.30	-0.20

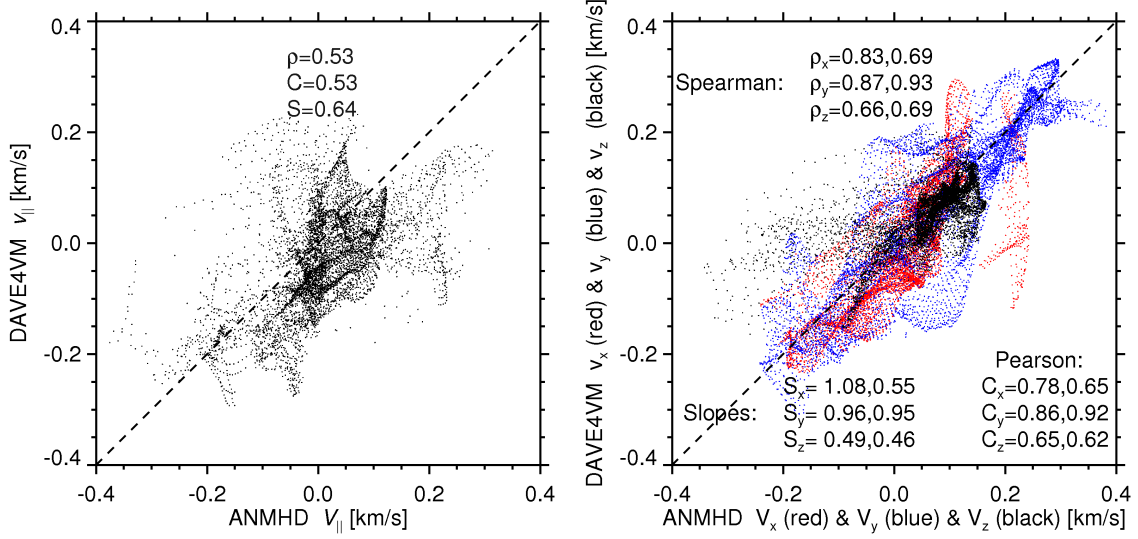


Fig. 7.— Scatter plots of (*left*) the estimated parallel plasma velocities v_{\parallel} from DAVE4VM versus the parallel plasma velocities V_{\parallel} from ANMHD and (*right*) the estimated *total* plasma velocity \mathbf{v} from DAVE4VM versus the *total* plasma velocities \mathbf{V} from ANMHD. The nonparametric Spearman rank-order correlation coefficients (ρ), Pearson correlation coefficients (C), and slopes (S) estimated by the least absolute deviation method are shown. The pairs of numbers represent correlations between \mathbf{v} and \mathbf{V} and \mathbf{v}_{\perp} and \mathbf{V} .

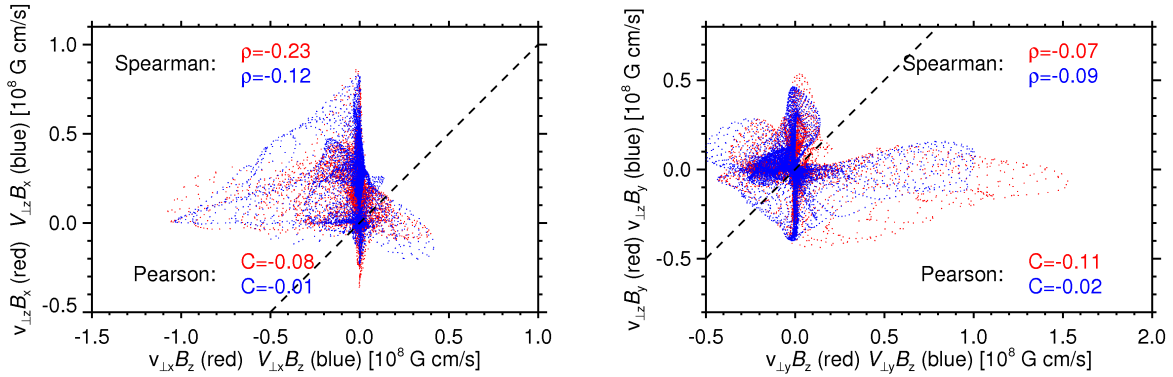


Fig. 8.— Scatterplots for the \hat{x} (*left*) and \hat{y} (*right*) components of (2a). The scatterplots indicate the *lack* of correlation between the terms describing shearing motion $B_z \mathbf{V}_h$ and emergence $V_z \mathbf{B}_h$. Red points indicate the results for DAVE4VM and blue points indicate the results for ANMHD. The Spearman rank order (ρ) and Pearson (C) correlations between the two terms are very low for both components of the flux transport velocities.

correlations than the DAVE4VM but the slopes are equivalent. For the DAVE4VM, the most significant deviations from the MHD induction equation occur near $\Delta B_z/\Delta t \approx 0$. Neither the DAVE nor DAVE4VM satisfy the induction equation exactly. This is by design, because real magnetogram data are likely to contain significant noise which will contaminate velocity estimates if the induction equation is satisfied exactly. Furthermore, how well a method satisfies the induction equation will generally depend on the differencing template. Consequently, if the velocity estimates are to be used as boundary values for ideal MHD coronal field models, then the velocities of any method will have to be adjusted to satisfy the induction equation on the differencing template implemented by the simulation. Using the Helmholtz decomposition (7), the inductive potential may be computed for the simulation directly from the magnetogram sequence (on the simulation differencing template)

$$\partial_t B_z = \nabla_h^2 \phi, \quad (24a)$$

and the electrostatic potential may be derived from the flux transport vectors determined by the optical flow method (Welsch et al. 2004)

$$\nabla_h^2 \psi = \hat{\mathbf{z}} \cdot [\nabla \times (\mathbf{u} B_z)]. \quad (24b)$$

Incorporating photospheric velocity estimate into boundary conditions for a coronal MHD simulation, in a minimally consistent way with the normal component of the magnetic induction equation, requires solving two Poisson equations on the photospheric boundary using the differencing template of the MHD code.

Figure 10 shows scatter plots of the estimated perpendicular electric fields \mathbf{e}_\perp from DAVE assuming $\boldsymbol{\vartheta} = \mathbf{u}$ (*left*) and from DAVE4VM (*right*) versus the electric fields \mathbf{E}_\perp from ANMHD. Red, blue, and black correspond to the x -, y -, and z -components, respectively. The nonparametric Spearman rank-order correlation coefficients (ρ) and Pearson correlation coefficients (C) are shown for each component of the electric field. On the present mask the DAVE4VM estimates improve or essentially match the correlation and slopes of the DAVE’s estimates for all three components of the electric field. Particularly dramatic is the improvement in the $\hat{\mathbf{y}}$ component of the electric field which the DAVE does not estimate accurately either on the present mask $|\mathbf{B}| > 370$ G or the restricted mask $|B_z| > 370$ G (Welsch et al. 2007).

3.3. Poynting and Helicity Fluxes

Démoulin & Berger (2003) show that the Poynting flux can be expressed concisely in terms of the flux transport vectors $\mathbf{u} B_z$

$$s_z(\mathbf{x}) = -\frac{1}{4\pi} \mathbf{B}_h \cdot (B_z \mathbf{v}_h - v_z \mathbf{B}_h) = -\frac{\mathbf{B}_h \cdot (\mathbf{u} B_z)}{4\pi}. \quad (25)$$

Figure 11 shows scatterplots of the estimated Poynting flux s_z from the DAVE assuming $\boldsymbol{\vartheta} = \mathbf{u}$ (*left*) and DAVE4VM (*right*) versus ANMHD’s Poynting flux S_z . The correspondence for DAVE4VM, or lack thereof for DAVE, indicates the accuracy of the velocity estimates in the direction of the horizontal magnetic field \mathbf{B}_h . The nonparametric Spearman rank-order correlation coefficients (ρ), Pearson correlation coefficients (C), and slopes (S) estimated by the least absolute deviation method are shown, as is the ratio of the integrated estimated Poynting flux to the integrated ANMHD Poynting flux $\mathcal{R}_{s_z} = \sum s_z / \sum S_z$. The DAVE4VM’s estimate of Poynting flux is a significant improvement over the DAVE’s. The correlations have improved by roughly a factor of 4 – 6, the slope has improved by nearly a factor of 18, and the ratio of the totals has improved by nearly a factor of 5. Again, DAVE does not reliably estimate the flux transport velocity in the direction of the horizontal magnetic field \mathbf{B}_h suggesting that DAVE is insensitive

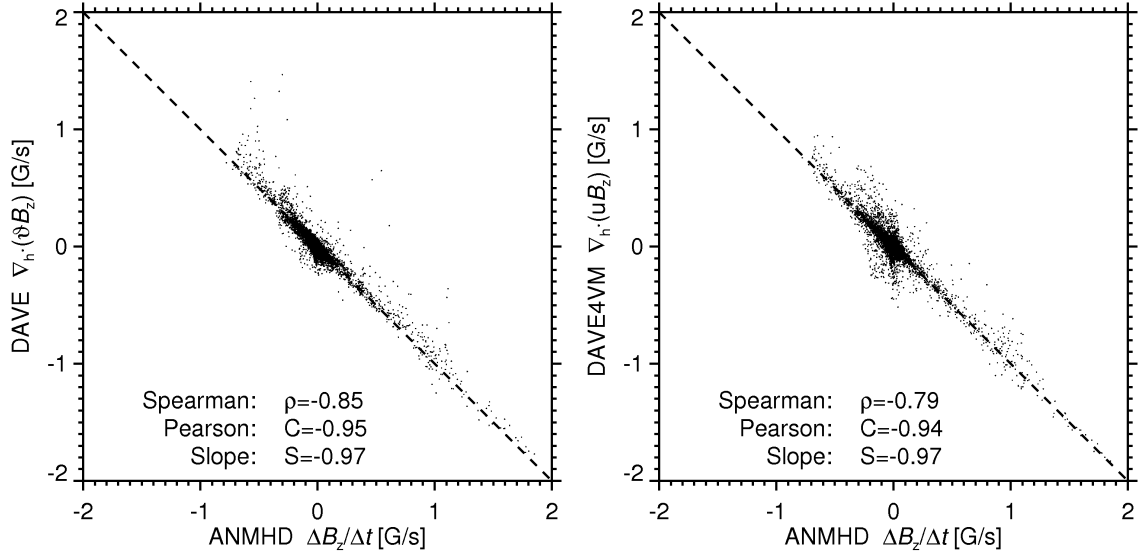


Fig. 9.— Scatter plots of $\nabla_h \cdot (\vartheta B_z)$ from the DAVE (*left*) and $\nabla_h \cdot (\mathbf{u} B_z)$ from the DAVE4VM (*right*) versus $\Delta B_z/\Delta t$ from ANMHD. The nonparametric Spearman rank-order correlation coefficients (ρ), Pearson correlation coefficients (C), and slopes (S) estimated by the least absolute deviation method are shown.

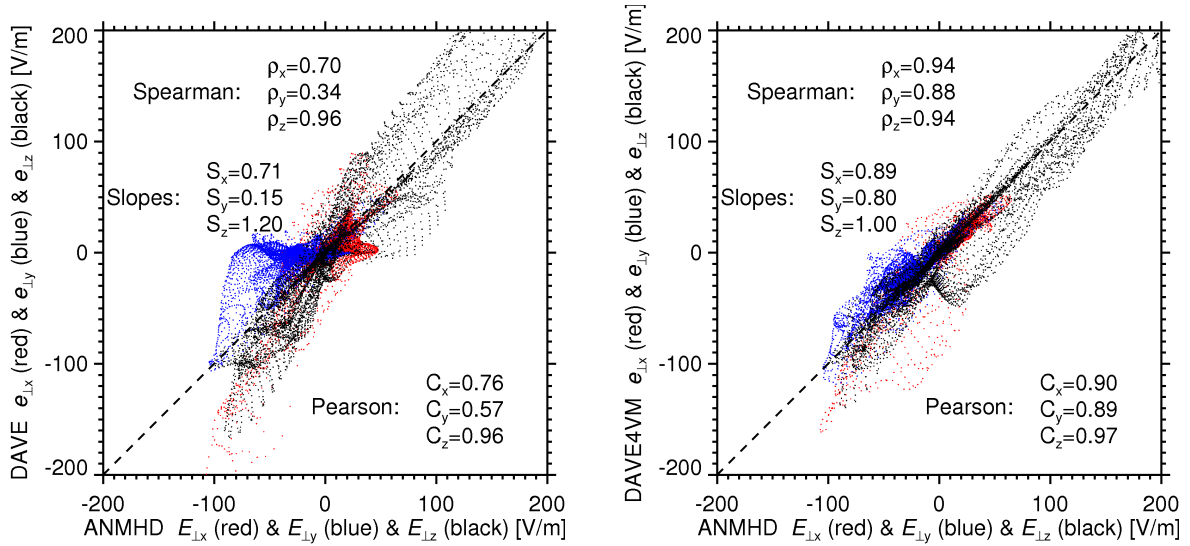


Fig. 10.— Scatter plots of the estimated perpendicular electric field \mathbf{e}_\perp from DAVE assuming $\vartheta = \mathbf{u}$ (*left*) and from DAVE4VM (*right*) versus the electric field \mathbf{E}_\perp from ANMHD. Red, blue, and black correspond to the x -, y -, and z -components respectively. The nonparametric Spearman rank-order correlation coefficients (ρ), Pearson correlation coefficients (C), and slopes (S) estimated by the least absolute deviation method are shown for each component of the electric field.

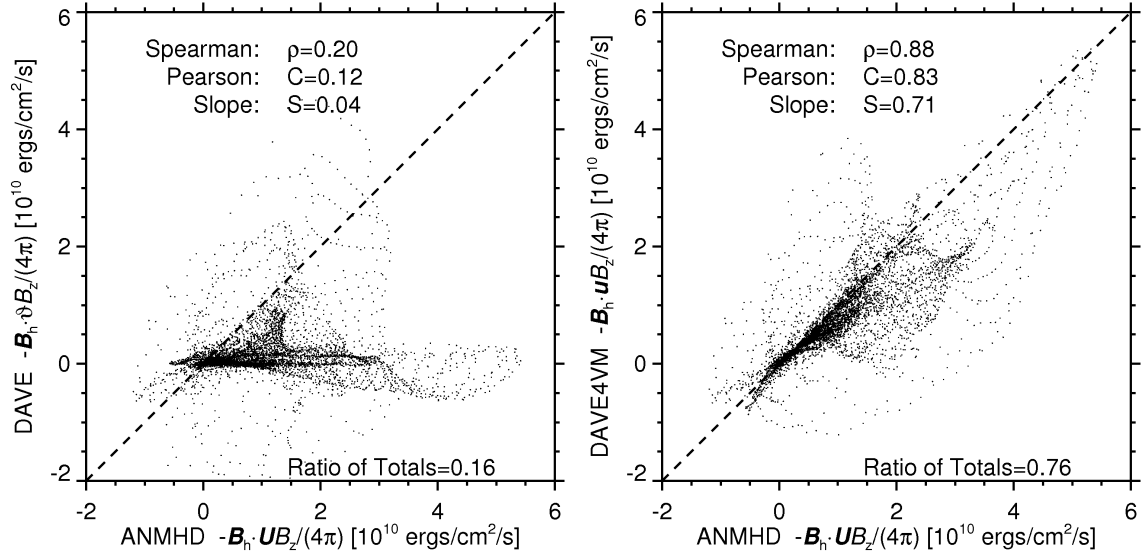


Fig. 11.— Scatter plots of the estimated Poynting flux from DAVE assuming $\mathbf{v} = \mathbf{u}$ (left) and DAVE4VM (right) versus the Poynting flux from ANMHD. The nonparametric Spearman rank-order correlation coefficients (ρ), Pearson correlation coefficients (C), and slopes (S) estimated by the least absolute deviation method are shown, as is the ratio of the integrated estimated Poynting flux to the integrated ANMHD Poynting flux.

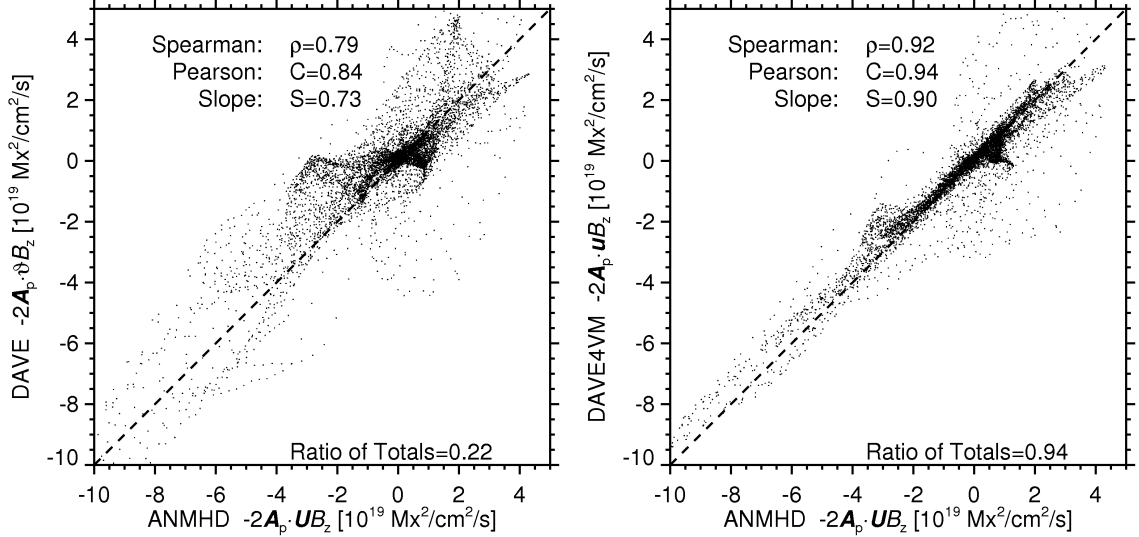


Fig. 12.— Scatter plots of the estimated helicity flux DAVE assuming $\mathbf{v} = \mathbf{u}$ (left) and DAVE4VM (right) versus ANMHD's helicity flux. The nonparametric Spearman rank-order correlation coefficients (ρ), Pearson correlation coefficients (C), and slopes (S) estimated by the least absolute deviation method are shown, as is the ratio of the integrated estimated helicity flux to the integrated ANMHD helicity flux.

to flux emergence which is proportional to $v_z \mathbf{B}_h$. The “ground truth” total power through the mask is $dP/dt = \sum S_z = 7.7 \times 10^{28}$ ergs/s.

Démoulin & Berger (2003) show that the gauge-invariant helicity flux (Berger & Field 1984) can be expressed concisely in terms of the flux transport vectors $\mathbf{u} B_z$

$$g_A(\mathbf{x}) = -2 \mathbf{A}_p \cdot (B_z \mathbf{v}_h - v_z \mathbf{B}_h) = -2 \mathbf{A}_p \cdot (\mathbf{u} B_z) \quad (26)$$

where $\mathbf{A}_p = \hat{\mathbf{z}} \times \nabla \Phi_p$ is the potential reference field (with zero helicity) which satisfies

$$\hat{\mathbf{z}} \cdot (\nabla \times \mathbf{A}_p) = \nabla_h^2 \Phi_p = B_z, \quad (27)$$

and $\nabla \cdot \mathbf{A}_p = \hat{\mathbf{z}} \cdot \mathbf{A}_p = 0$. To estimate the helicity flux density, Φ_p was computed on a 257×257 square centered on the region of interest with Dirichlet boundary conditions using MUDPACK (Adams 1993). While interpretation of maps of helicity flux $g_A(\mathbf{x})$ through the photosphere is problematic (Pariat et al. 2005, 2007), a comparison of $g_A(\mathbf{x})$ estimated from the DAVE or DAVE4VM versus $G_A(\mathbf{x})$ calculated from ANMHD indicates the *accuracy* of the estimated flux transport vectors in the direction of the vector potential. Figure 12 shows scatter plots of the estimated helicity flux from DAVE assuming $\boldsymbol{\vartheta} = \mathbf{u}$ (*left*) and DAVE4VM (*right*) versus ANMHD’s helicity flux. The nonparametric Spearman rank-order correlation coefficients (ρ) and Pearson correlation coefficients (C) are shown, as is the ratio of the integrated estimated helicity flux to the integrated ANMHD helicity flux $\mathcal{R}_{g_A} = \sum g_A / \sum G_A$. The DAVE4VM’s estimates represent a significant improvement over the DAVE’s, improving the correlation coefficients by roughly 0.1 and the slope by 0.2. Furthermore, the ratio of totals has improved by roughly a factor of 4 from 0.22 for the DAVE to 0.94 for the DAVE4VM. The “ground truth”³ helicity injected through the surface is $dH_A/dt = \sum G_A = -2.8 \times 10^{37}$ Mx²/s.

4. Discussion and Conclusions

For completeness, Tables 4 and 5 provide a summary of metrics and correlation coefficients for the DAVE and DAVE4VM on the original mask $|B_z| > 370$ G used by Welsch et al. (2007) in the same format as in Tables 1 and 2. MEF performed the best overall in the original study by Welsch et al. (2007) although there were some metrics where the DAVE outperformed MEF such as in the accuracy of the plasma velocities listed in Table 5 (compare with Figure 8 in Welsch et al. (2007)). The DAVE4VM’s estimates are a substantial improvement over the results of the DAVE assuming $\boldsymbol{\vartheta} = \mathbf{u}$ on this mask. Comparing the rank-order Spearman correlation coefficients for the flux transport vectors, perpendicular plasma velocity, and electric field in Table 4, the DAVE4VM equals or out-performs MEF. Particularly, the DAVE4VM’s estimate of the vertical perpendicular plasma velocity is substantially better than MEF with a rank-order of 0.76 in the former and 0.61 in the latter case. Accurate vertical flows are necessary to diagnose flux emergence and accurately estimate the helicity flux. The one area where MEF exhibits superiority is in the estimate of the Poynting flux where the DAVE4VM captures 76% and MEF captures 100% (Welsch et al. 2007). The fractional errors $\langle |\delta \tilde{\mathbf{f}}| \rangle$ and $\langle \delta |\tilde{\mathbf{f}}| \rangle$ are substantially lower than the DAVE for both the flux transport vectors and plasma velocities. The DAVE had the largest vector correlation C_{vec} and the direction correlation C_{CS} in the original study and the DAVE4VM improves over this performance exhibiting correlation coefficients of

³This estimate differs by about 10% from the helicity estimate in Welsch et al. (2007). The discrepancy is caused by the different methodologies and boundaries used for computing the vector potential \mathbf{A}_p . MUDPACK was used in this study with (27) whereas Welsch et al. (2007) used a Green’s function scheme to compute \mathbf{A}_p .

Table 4. Comparison between the DAVE and DAVE4VM over the 3815 pixels that satisfy $|B_z| > 370$ G in Figure 2. This corresponds roughly to the mask used in Welsch et al. (2007).

Quantities		DAVE (Assuming $\boldsymbol{\vartheta} = \boldsymbol{u}$)			DAVE4VM		
		Spearman	Pearson	Slope	Spearman	Pearson	Slope
$u_x B_z$	$U_x B_z$	0.43	0.60	0.33	0.87	0.88	0.81
$u_y B_z$	$U_y B_z$	0.73	0.86	1.07	0.90	0.90	0.95
$v_{\perp x}$	$V_{\perp x}$	0.88	0.91	0.86	0.90	0.92	0.93
$v_{\perp y}$	$V_{\perp y}$	0.93	0.93	1.17	0.93	0.93	0.99
$v_{\perp z}$	$V_{\perp z}$	0.27	0.39	0.29	0.76	0.77	0.72
$\nabla_h \cdot (\boldsymbol{u} B_z)$	$\Delta B_z / \Delta t$	-0.92	-0.95	-0.99	-0.84	-0.95	-0.97
$e_{\perp x}$	$E_{\perp x}$	0.73	0.86	1.07	0.90	0.90	0.95
$e_{\perp y}$	$E_{\perp y}$	0.43	0.60	0.33	0.87	0.88	0.81
$e_{\perp z}$	$E_{\perp z}$	0.97	0.96	1.17	0.96	0.97	0.98
s_z	S_z	0.09	0.05	0.02	0.83	0.79	0.68

Table 5. Comparison of accuracy of the velocity estimates between the DAVE and DAVE4VM over the 3815 pixels that satisfy $|B_z| > 370$ G in Figure 2. This corresponds roughly to the mask used in Welsch et al. (2007).

\boldsymbol{f}	DAVE (Assuming $\boldsymbol{\vartheta} = \boldsymbol{u}$)					DAVE4VM				
	$\langle \delta \tilde{\boldsymbol{f}} \rangle$	$\langle \delta \tilde{\boldsymbol{f}} \rangle$	C_{vec}	C_{CS}	$\langle \cos \theta \rangle_W$	$\langle \delta \tilde{\boldsymbol{f}} \rangle$	$\langle \delta \tilde{\boldsymbol{f}} \rangle$	C_{vec}	C_{CS}	$\langle \cos \theta \rangle_W$
$\boldsymbol{u} B_z$	0.75 ± 0.37	-0.26 ± 0.40	0.68	0.69	0.74	0.42 ± 0.30	-0.08 ± 0.24	0.91	0.91	0.93
\boldsymbol{v}_{\perp}	0.57 ± 0.30	0.06 ± 0.27	0.87	0.87	0.88	0.39 ± 0.28	-0.01 ± 0.17	0.93	0.90	0.92

roughly 0.9. The improvement for the flux transport vectors is particularly dramatic. The plasma velocities are more accurate and exhibit considerably less bias than those reported for MEF in Welsch et al. (2007).

The DAVE4VM offers some minor advantages over MEF. The DAVE4VM is somewhat faster than MEF; the DAVE4VM(DAVE) requires 30(10) seconds to process⁴ the full 288×288 pixel frame from ANMHD whereas MEF requires roughly 10 minutes to converge on a reduced mask of the ANMHD data (private communication with Belur Ravindra). The DAVEVM is local and directly estimates velocities across neutral lines and across broader weak field regions whereas MEF is an iterative global method that requires judicious choice of boundaries to ensure convergence. In concert, the DAVE4VM’s velocity estimate might be used with MEF either as an initial guess for the electrostatic potential ψ via (24b) or as ancillary inaccurate velocity measurements in the MEF variational term that constrains the photospheric plasma velocities (Longcope 2004). Since the DAVE4VM is fast and does not require supervision beyond choosing a window size (and even this could be automated according to the criteria discussed in § 3), this approach is appropriate for real-time monitoring of helicity and energy fluxes through the photosphere from observatories such as *Solar Dynamics Observatory*.

What is responsible for the DAVE4VM’s improved performance? The only differences between the DAVE and DAVE4VM are the terms s_{ij} in the structure tensor (14) that describe the local structure of the horizontal magnetic fields necessary for the description of vertical flows. There are two circumstances when line-of-sight methods such as the DAVE, LMSAL’s LCT, and FLCT will produce accurate estimates of the flux transport velocity:

1. $\mathbf{B}_h = 0$: *The magnetic field is purely vertical* and $\boldsymbol{\vartheta} = \mathbf{v}_h = \mathbf{v}_{\perp h}$. If the horizontal magnetic fields and their associated derivatives are zeroed, the DAVE and DAVE4VM produce *identical* flux transport and perpendicular plasma velocity estimates. The DAVE is consistent with the assumption that the magnetic field is purely vertical:

$$\lim_{\mathbf{B}_h \rightarrow 0} \partial_t B_z + \nabla_h \cdot (B_z \mathbf{v}_h - v_z \mathbf{B}_h) = \partial_t B_z + \nabla_h \cdot (B_z \mathbf{v}_h). \quad (28a)$$

2. $v_z = 0$: *There are no net upflow/downflows* and $\boldsymbol{\vartheta} = \mathbf{v}_h \neq \mathbf{v}_{\perp h}$. In this situation, there must be projected vertical flows along the magnetic field to cancel any projected vertical flow perpendicular to the magnetic field with $v_{\perp z} = -v_{\parallel z} = -B_z (\mathbf{v}_h \cdot \mathbf{B}_h) / B^2$. Consequently, $\mathbf{v}_{\parallel} \neq 0$. The DAVE is consistent with the assumption that there are no vertical flows $v_z = 0$:

$$\lim_{v_z \rightarrow 0} \partial_t B_z + \nabla_h \cdot (B_z \mathbf{v}_h - v_z \mathbf{B}_h) = \partial_t B_z + \nabla_h \cdot (B_z \mathbf{v}_h). \quad (28b)$$

Both limits (28a) and (28b) are isomorphic with (6). By induction, (6) is consistent with the assumptions leading to (28a) and (28b). Since DAVE does not consider corrections s_{ij} due to the horizontal magnetic field, $\boldsymbol{\vartheta}$ *should generally be considered a biased estimate of the horizontal plasma velocity* $\boldsymbol{\vartheta} = \mathbf{v}_h$ *and not the flux transport velocity!* Formally the alternative hypothesis $H_1 : \boldsymbol{\vartheta} = \mathbf{v}_h$ may be tested against the null hypothesis $H_0 : \boldsymbol{\vartheta} = \mathbf{u}$ of Démoulin & Berger (2003). The null hypothesis $H_0 : \boldsymbol{\vartheta} = \mathbf{u}$ is represented by the left panel in Figure 3. The alternative hypothesis, represented by $H_1 : \boldsymbol{\vartheta} = \mathbf{v}_h$, is characterized by the scatter

⁴The routines were all coded in Interactive Data Language (IDL 2002) and the computations were performed on a dual processor AMD Opteron 240 running at 1.4 GHz with a one megabyte memory cache and ten gigabytes of Random Access Memory.

plot of the estimated velocities $\boldsymbol{\vartheta} B_z$ for DAVE versus the horizontal plasma velocities $\mathbf{V}_h B_z$ from ANMHD in Figure 13. The nonparametric Spearman rank-order correlation coefficients (ρ), Pearson correlation coefficients (C), and slopes (S) estimated by the least absolute deviation method are all significantly better for the alternative hypothesis than for the null hypothesis. The null hypothesis that the velocities inferred by DAVE represent the flux transport velocities may be rejected in favor⁵ of the alternative hypothesis $\boldsymbol{\vartheta} = \mathbf{v}_h$.

These results explain why $V_{\perp z}$ and $v_{\perp z}$ are poorly correlated for the DAVE in Figure 4 and the slope between them is nearly zero — the DAVE is consistent with the *assumption* $v_z = 0$ when $\mathbf{B}_h \neq 0$. Generally, in regions of flux emergence, the accuracy $v_{\perp z}$ is critical for estimating the flux transport vectors which in turn is critical for estimating the helicity and Poynting fluxes. When horizontal magnetic fields and vertical flows are present, the flux transport vectors estimated from methods that rely exclusively on the line-of-sight or vertical component (DAVE, LMSAL’s LCT, FLCT) cannot be trusted to provide the total fluxes. This is particularly true along neutral lines where flux is emerging or submerging! Under the *best case scenarios*, only the shearing or “horizontal fluxes”⁶ across the photosphere.

$$\left. \frac{dp}{dt} \right|_h = -\frac{1}{4\pi} \int_S dx^2 \mathbf{B}_h \cdot (\mathbf{v}_h B_z), \quad (29a)$$

and

$$\left. \frac{dh_A}{dt} \right|_h = -2 \int_S dx^2 \mathbf{A}_p \cdot (\mathbf{v}_h B_z), \quad (29b)$$

may be estimated from the line-of-sight tracking methods. In the best case scenarios only the shearing fluxes are captured by line-of-sight tracking methods in *partial* agreement with the *Ansatz* of Chae (2001) and in disagreement with the geometrical arguments of Démoulin & Berger (2003) who argue that line-of-sight tracking methods capture both the shearing and emergence. Again, for the energy and helicity, the alternative hypothesis $H_1 : \boldsymbol{\vartheta} = \mathbf{v}_h$ (shearing) may be tested against the null hypothesis $H_0 : \boldsymbol{\vartheta} = \mathbf{u}$ (shearing and emergence). The left panel of Figure 14, representing the null hypothesis is a combination of the left-hand panels of Figure 11 and Figure 12. The right panel of Figure 14, representing the alternative hypothesis, combines the shearing term estimated from DAVE with the emergence term from ANMHD. Generally, in the presence of vertical flows and horizontal magnetic fields, line-of-sight tracking methods do not accurately capture the complete footpoint dynamics and the null hypothesis that the velocities inferred by DAVE represent the flux transport velocities may be rejected in favor of the alternative hypothesis $\boldsymbol{\vartheta} = \mathbf{v}_h$.

The implementation of vector magnetograms in optical flow methods presents practical challenges. First, the transverse magnetic field components are known to be noisier than the line-of-sight component and the noise variance will likely change from pixel to pixel due to variable photon statistics (heteroscedastic errors). Second the line-of-sight component and transverse components are determined from different polarizations and require inter-calibration. Third, the orientation of the transverse component is ambiguous by 180° . The first issue may be addressed within the total least squares framework discussed by Schuck (2006), Branham Jr. (1999) and others (See references in Schuck 2006). The main obstacle to resolving the first issue is estimating a covariance matrix for the structure tensor $\langle \mathbf{S} \rangle$.

The second and third issues both may be interpreted as inter-calibration bias where the estimated horizontal magnetic field $\hat{\mathbf{B}}_h = \alpha \mathbf{B}_h$ is proportional to the true horizontal magnetic field \mathbf{B}_h ; these errors are

⁵This does not imply that the alternative hypothesis is correct.

⁶Démoulin & Berger (2003) terms these fluxes the “tangential fluxes” but “horizontal” is more appropriate in the context of Welsch’s terminology used in this paper.

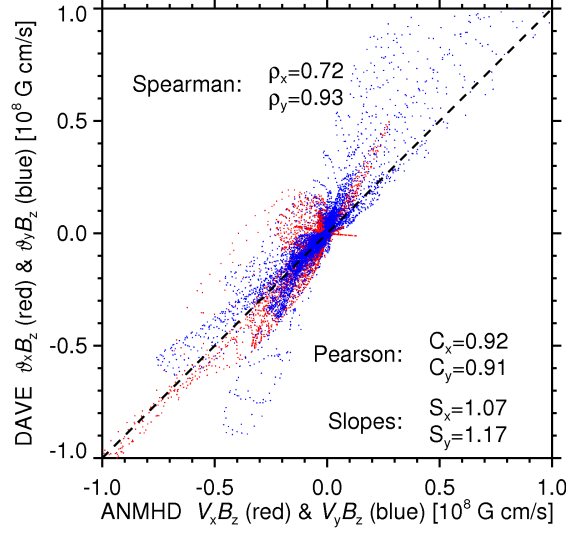


Fig. 13.— Scatter plots of the estimated velocities ϑB_z from DAVE versus the horizontal plasma velocities $V_h B_z$ from ANMHD. The nonparametric Spearman rank-order correlation coefficients (ρ), Pearson correlation coefficients (C), and slopes (S) estimated by the least absolute deviation method are shown.

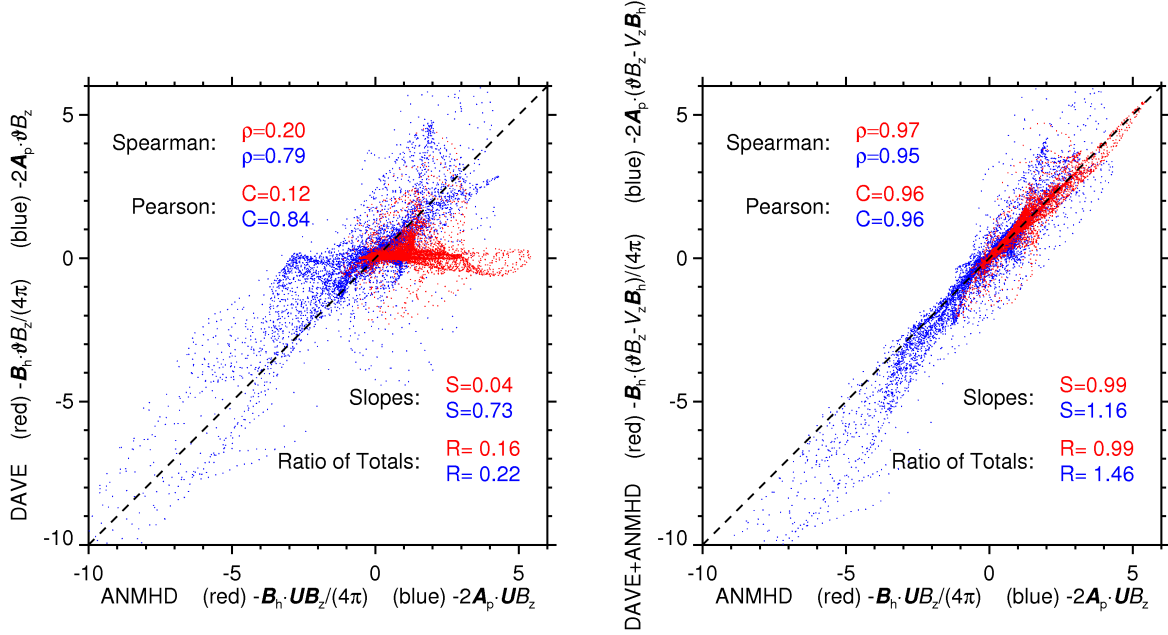


Fig. 14.— (*left*) Scatter plots of the estimated Poynting flux (red) and helicity flux (blue) from DAVE assuming $\vartheta = u$ versus the Poynting and helicity flux from ANMHD. (*right*) Scatter plots of the estimated Poynting flux (red) and helicity flux (blue) combining DAVE assuming $\vartheta = v_h$ with the emergence term from ANMHD versus the Poynting and helicity flux from ANMHD. The nonparametric Spearman rank-order correlation coefficients (ρ), Pearson correlation coefficients (C), and slopes (S) estimated by the least absolute deviation method are shown.

not random. The flux transport velocities estimated from DAVE4VM are robust to *overall* inter-calibration errors which include the 180° ambiguity resolution errors. Changing the *overall* magnitude or sign of \mathbf{B}_h has no effect on the flux transport velocities because (5a) is invariant with respect to the transformation $v_z \rightarrow v_z/\alpha$ and $\mathbf{B}_h \rightarrow \alpha\mathbf{B}_h$ (private communication with Pascal Demoulin). However, the estimated vertical perpendicular plasma velocity and vertical perpendicular electric field will be anti-correlated with the ground truth when $\alpha < 0$. Nonetheless, an *overall* rescaling of the horizontal magnetic field will have no effect on the helicity flux. However, the Poynting flux will be incorrect by a factor of α including perhaps a sign error because of the rescaling horizontal magnetic field which is inherent in the energy estimate (25). More troublesome are the effects of *spatially varying* bias errors in inter-calibration or ambiguity resolution. The consequences of these errors, particularly along the boundaries between proper and improper ambiguity resolution, are presently unknown and should be investigated with future end-to-end analysis of synthetic magnetograms. However, local methods such as DAVE4VM are probably more robust than global methods to spatially dependent errors in inter-calibration or ambiguity resolution because local methods inherently localize the effect of bias errors by isolating subregions with the window aperture whereas global methods couple the entire solution region together permitting bias errors in one subregion to influence the solution in other subregions.

In light of the DAVE4VM’s dramatic improvement in performance by simply including horizontal magnetic fields, speculation that the ANMHD simulation data are not appropriate for testing tracking methods cannot be correct. Rather, aside from issues of image structure, the ANMHD simulation data represent an *ideal* case for the line-of-sight methods because the vertical magnetic field is known (not simply the line-of-sight component). The results of this study suggest that horizontal magnetic fields and vertical flows will render velocity estimates from “pure” tracking methods inaccurate if they are treated as the flux transport velocities \mathbf{u} . This conclusion holds equally true for velocity estimates near disk center as the ANMHD simulations represents disk-center data! The good agreement between the performance of MEF and the DAVE4VM on the ANMHD data implies that incorporating the right physics is more important for producing accurate velocity estimates than is the particular method used to solve the equations.

Presently, the *only* way to explore the “image” physics is by testing the “optical flow” methods on synthetic data from well-designed MHD simulations that attempt to reproduce the physics of the Sun. Naive “moving paint” experiments (Schuck 2006) cannot critically test optical flow methods for magnetograms because the test data are consistent with the two circumstances when pure tracking methods will certainly perform well: $\mathbf{B}_h = 0$ and $v_z = 0$. Consequently, good performance of an optical flow method in naive “moving paint” experiments should not be considered evidence that a method will produce accurate estimates of plasma physics quantities.

In the interest of reproducibility (Joyner & Stein 2007), all of the software used to perform the calculations, create the figures, and draw the conclusions for this paper are archived with the *Astrophysical Journal* as a `tgz` file. Updates to the DAVE/DAVE4VM software are also available.⁷

I thank the referee for constructive criticism, Graham Barnes for encouraging the publication of this work, Bill Abbett for providing the ANMHD data that formed the core of this research, and Pascal Demoulin and Brian Welsch for encouraging the clarification of several issues discussed in this manuscript. I also gratefully acknowledge useful conversations with George Fisher, Bill Amatucci, and Etienne Pariat. I thank Julie Schuck for editing the manuscript. This work was supported by NASA LWS TR&T grant NNH06AD87I,

⁷<http://wwwppd.nrl.navy.mil/whatsnew/>.

LWS TR&T Strategic Capability grant NNH07AG26I, and ONR.

A. Matrix Elements of \mathbf{S}

$$\begin{aligned}
\mathcal{G}_{00} &= (\partial_x B_z)^2 \\
\mathcal{G}_{10} &= (\partial_x B_z) (\partial_y B_z) \\
\mathcal{G}_{11} &= (\partial_y B_z)^2 \\
\mathcal{G}_{20} &= B_z (\partial_x B_z) + (\partial_x B_z)^2 x' \\
\mathcal{G}_{21} &= B_z (\partial_y B_z) + (\partial_x B_z) (\partial_y B_z) x' \\
\mathcal{G}_{22} &= B_z^2 + 2 B_z (\partial_x B_z) x' + (\partial_x B_z)^2 x'^2 \\
\mathcal{G}_{30} &= B_z (\partial_x B_z) + (\partial_x B_z) (\partial_y B_z) y' \\
\mathcal{G}_{31} &= B_z (\partial_y B_z) + (\partial_y B_z)^2 y' \\
\mathcal{G}_{32} &= B_z^2 + B_z (\partial_x B_z) x' + B_z (\partial_y B_z) y' + (\partial_x B_z) (\partial_y B_z) x' y' \\
\mathcal{G}_{33} &= B_z^2 + 2 B_z (\partial_y B_z) y' + (\partial_y B_z)^2 y'^2 \\
\mathcal{G}_{40} &= (\partial_x B_z)^2 y' \\
\mathcal{G}_{41} &= (\partial_x B_z) (\partial_y B_z) y' \\
\mathcal{G}_{42} &= B_z (\partial_x B_z) y' + (\partial_x B_z)^2 x' y' \\
\mathcal{G}_{43} &= B_z (\partial_x B_z) y' + (\partial_x B_z) (\partial_y B_z) y'^2 \\
\mathcal{G}_{44} &= (\partial_x B_z)^2 y'^2 \\
\mathcal{G}_{50} &= (\partial_x B_z) (\partial_y B_z) x' \\
\mathcal{G}_{51} &= (\partial_y B_z)^2 x' \\
\mathcal{G}_{52} &= B_z (\partial_y B_z) x' + (\partial_x B_z) (\partial_y B_z) x'^2 \\
\mathcal{G}_{53} &= B_z (\partial_y B_z) x' + (\partial_y B_z)^2 x' y' \\
\mathcal{G}_{54} &= (\partial_x B_z) (\partial_y B_z) x' y' \\
\mathcal{G}_{55} &= (\partial_y B_z)^2 x'^2 \\
\mathbf{s}_{60} &= -(\partial_x B_x) (\partial_x B_z) - (\partial_y B_z) (\partial_x B_z) \\
\mathbf{s}_{61} &= -(\partial_x B_x) (\partial_y B_z) - (\partial_y B_z) (\partial_y B_z) \\
\mathbf{s}_{62} &= -(\partial_x B_x) B_z - (\partial_y B_z) B_z - (\partial_x B_x) (\partial_x B_z) x' - (\partial_y B_z) (\partial_x B_z) x' \\
\mathbf{s}_{63} &= -(\partial_x B_x) B_z - (\partial_y B_z) B_z - (\partial_x B_x) (\partial_y B_z) y' - (\partial_y B_z) (\partial_y B_z) y' \\
\mathbf{s}_{64} &= -(\partial_x B_x) (\partial_x B_z) y' - (\partial_y B_z) (\partial_x B_z) y' \\
\mathbf{s}_{65} &= -(\partial_x B_x) (\partial_y B_z) x' - (\partial_y B_z) (\partial_y B_z) x' \\
\mathbf{s}_{66} &= (\partial_x B_x)^2 + 2 (\partial_x B_x) (\partial_y B_z) + (\partial_y B_z)^2 \\
\mathbf{s}_{70} &= -B_x (\partial_x B_z) - (\partial_x B_x) (\partial_x B_z) x' - (\partial_y B_z) (\partial_x B_z) x' \\
\mathbf{s}_{71} &= -B_x (\partial_y B_z) - (\partial_x B_x) (\partial_y B_z) x' - (\partial_y B_z) (\partial_y B_z) x' \\
\mathbf{s}_{72} &= -B_x B_z - (\partial_x B_x) B_z x' - (\partial_y B_z) B_z x' - B_x (\partial_x B_z) x' - (\partial_x B_x) (\partial_x B_z) x'^2 - (\partial_y B_z) (\partial_x B_z) x'^2 \\
\mathbf{s}_{73} &= -B_x B_z - (\partial_x B_x) B_z x' - (\partial_y B_z) B_z x' - B_x (\partial_y B_z) y' - (\partial_x B_x) (\partial_y B_z) x' y' - (\partial_y B_z) (\partial_y B_z) x' y'
\end{aligned}$$

$$\begin{aligned}
s_{74} &= -B_x (\partial_x B_z) y' - (\partial_x B_x) (\partial_x B_z) x' y' - (\partial_y B_z) (\partial_x B_z) x' y' \\
s_{75} &= -B_x (\partial_y B_z) x' - (\partial_x B_x) (\partial_y B_z) x'^2 - (\partial_y B_z) (\partial_y B_z) x'^2 \\
s_{76} &= B_x (\partial_x B_x) + B_x (\partial_y B_z) + (\partial_x B_x)^2 x' + 2 (\partial_x B_x) (\partial_y B_z) x' + (\partial_y B_z)^2 x' \\
s_{77} &= B_x^2 + 2 B_x (\partial_x B_x) x' + 2 B_x (\partial_y B_z) x' + (\partial_x B_x)^2 x'^2 + 2 (\partial_x B_x) (\partial_y B_z) x'^2 + (\partial_y B_z)^2 x'^2 \\
s_{80} &= -B_y (\partial_x B_z) - (\partial_x B_x) (\partial_x B_z) y' - (\partial_y B_z) (\partial_x B_z) y' \\
s_{81} &= -B_y (\partial_y B_z) - (\partial_x B_x) (\partial_y B_z) y' - (\partial_y B_z) (\partial_y B_z) y' \\
s_{82} &= -B_y B_z - B_y (\partial_x B_z) x' - (\partial_x B_x) B_z y' - (\partial_y B_z) B_z y' - (\partial_x B_x) (\partial_x B_z) x' y' - (\partial_y B_z) (\partial_x B_z) x' y' \\
s_{83} &= -B_y B_z - (\partial_x B_x) B_z y' - (\partial_y B_z) B_z y' - B_y (\partial_y B_z) y' - (\partial_x B_x) (\partial_y B_z) y'^2 - (\partial_y B_z) (\partial_y B_z) y'^2 \\
s_{84} &= -B_y (\partial_x B_z) y' - (\partial_x B_x) (\partial_x B_z) y'^2 - (\partial_y B_z) (\partial_x B_z) y'^2 \\
s_{85} &= -B_y (\partial_y B_z) x' - (\partial_x B_x) (\partial_y B_z) x' y' - (\partial_y B_z) (\partial_y B_z) x' y' \\
s_{86} &= (\partial_x B_x) B_y + B_y (\partial_y B_z) + (\partial_x B_x)^2 y' + 2 (\partial_x B_x) (\partial_y B_z) y' + (\partial_y B_z)^2 y' \\
s_{87} &= B_x B_y + (\partial_x B_x) B_y x' + B_y (\partial_y B_z) x' + B_x (\partial_x B_x) y' + B_x (\partial_y B_z) y' \\
&\quad + (\partial_x B_x)^2 x' y' + 2 (\partial_x B_x) (\partial_y B_z) x' y' + (\partial_y B_z)^2 x' y' \\
s_{88} &= B_y^2 + 2 (\partial_x B_x) B_y y' + 2 B_y (\partial_y B_z) y' + (\partial_x B_x)^2 y'^2 + 2 (\partial_x B_x) (\partial_y B_z) y'^2 + (\partial_y B_z)^2 y'^2 \\
\mathcal{G}_{90} &= (\partial_t B_z) (\partial_x B_z) \\
\mathcal{G}_{91} &= (\partial_t B_z) (\partial_y B_z) \\
\mathcal{G}_{92} &= B_z (\partial_t B_z) + (\partial_t B_z) (\partial_x B_z) x' \\
\mathcal{G}_{93} &= B_z (\partial_t B_z) + (\partial_t B_z) (\partial_y B_z) y' \\
\mathcal{G}_{94} &= (\partial_t B_z) (\partial_x B_z) y' \\
\mathcal{G}_{95} &= (\partial_t B_z) (\partial_y B_z) x' \\
s_{96} &= -(\partial_x B_x) (\partial_t B_z) - (\partial_y B_z) (\partial_t B_z) \\
s_{97} &= -B_x (\partial_t B_z) - (\partial_x B_x) (\partial_t B_z) x' - (\partial_y B_z) (\partial_t B_z) x' \\
s_{98} &= -B_y (\partial_t B_z) - (\partial_x B_x) (\partial_t B_z) y' - (\partial_y B_z) (\partial_t B_z) y' \\
\mathcal{G}_{99} &= (\partial_t B_z)^2
\end{aligned}$$

The primed coordinates are defined relative to the center of the aperture $\mathbf{x}' = \mathbf{x} - \boldsymbol{\chi}$.

REFERENCES

- Abbett, W. P., Fisher, G. H., & Fan, Y. 2000, ApJ, 540, 548
- Abbett, W. P., Fisher, G. H., Fan, Y., & Bercik, D. J. 2004, ApJ, 612, 557
- Adams, J. C. 1993, Appl. Math. Comput., 53, 235, <http://www.cisl.ucar.edu/css/software/mudpack/>
- Amari, T., Luciani, J. F., Aly, J. J., Mikic, Z., & Linker, J. 2003a, ApJ, 585, 1073
- . 2003b, ApJ, 595, 1231
- Amari, T., Luciani, J. F., Mikic, Z., & Linker, J. 2000, ApJ, 529, L49
- Antiochos, S. K., DeVore, C. R., & Klimchuk, J. A. 1999, ApJ, 510, 485

- Baker, S., & Matthews, I. 2004, *Int. J. Comp. Vision*, 56, 221,
http://www.ri.cmu.edu/projects/project_515.html
- Berger, M. A., & Field, G. B. 1984, *Journal of Fluid Mechanics*, 147
- Berger, M. A., & Ruzmaikin, A. 2000, *J. Geophys. Res.*, 105, 10481
- Branham Jr., R. L. 1999, *The Astronomical Journal*, 117, 1942
- Chae, J. 2001, *ApJ*, 560, L95
- . 2007, *Advances in Space Research*, 39, 1700
- Chae, J., Wang, H., Qiu, J., Goode, P. R., Strous, L., & Yun, H. S. 2001, *ApJ*, 560, 476
- Chen, J. 1989, *ApJ*, 338, 453
- . 1996, *J. Geophys. Res.*, 101, 27499
- Démoulin, P., & Berger, M. A. 2003, *Sol. Phys.*, 215, 203
- DeRosa, M. L. 2001, PhD thesis, Univ. of Colorado
- Fan, Y., Zweibel, E. G., Linton, M. G., & Fisher, G. H. 1999, *ApJ*, 521, 460
- Fieller, E. C., Hartley, H. O., & Pearson, E. S. 1957, *Biometrika*, 44, 470
- Georgoulis, M. K., & LaBonte, B. J. 2006, *ApJ*, 636, 475
- Golub, G. H., & Van Loan, C. F. 1980, *SIAM J. Num. Anal.*, 17, 883
- Gosling, J. T. 1993, *J. Geophys. Res.*, 98, 18937
- Hildreth, E. C. 1983, *Proc. Royal. Soc. London*, 221, 189
- . 1984, *Measurement of Visual Motion* (MIT Press)
- IDL. 2002, *IDL Reference Guide* (Research Systems, Inc.), <http://www.rsinc.com/idl/>
- Jähne, B. 2004, *Practical handbook on image processing for scientific and technical applications*, 2nd edn. (Boca Raton, Fla.: CRC Press)
- Joyner, D., & Stein, W. 2007, *Notices of the AMS*, 54, 1279
- Kliem, B., Titov, V. S., & Török, T. 2004, *A&A*, 413, L23
- Kusano, K., Maeshiro, T., Yokoyama, T., & Sakurai, T. 2002, *ApJ*, 577, 501
- Kusano, K., Maeshiro, T., Yokoyama, T., & Sakurai, T. 2004, in *ASP Conf. Ser. 325: The Solar-B Mission and the Forefront of Solar Physics*, 175–+
- LaBonte, B. J., Georgoulis, M. K., & Rust, D. M. 2007, *ApJ*, 671, 955
- Leese, J. A., Novak, C. S., & Clark, B. B. 1971, *Journal of Applied Meteorology*, 10, 118
- Leese, J. A., Novak, C. S., & Taylor, V. R. 1970, *Pattern Recognition*, 2, 279

- Leka, K. D., & Barnes, G. 2003a, *ApJ*, 595, 1277
- . 2003b, *ApJ*, 595, 1296
- . 2007, *ApJ*, 656, 1173
- Linker, J. A., Lionello, R., Mikić, Z., & Amari, T. 2001, *J. Geophys. Res.*, 106, 25165
- Litvinenko, Y. E., Chae, J., & Park, S.-Y. 2007, *ApJ*, 662, 1302
- Longcope, D. W. 2004, *ApJ*, 612, 1181
- Lucas, B. 1984, PhD thesis, Carnegie-Mellon University
- Lucas, B., & Kanade, T. 1981, in *Proceedings of the 7th International Joint Conference on Artificial Intelligence (IJCAI '81)*, Vancouver, BC, Canada, August 1981, ed. P. J. Hayes (Los Altos, CA: William Kaufmann), 674–679
- Marr, D., & Ullman, S. 1981, *Proc. R. Soc. Lond. B*, 211, 151
- Metcalf, T. R., Derosa, M. L., Schrijver, C. J., Barnes, G., van Ballegoijen, A. A., Wiegmann, T., Wheatland, M. S., Valori, G., & McTiernan, J. M. 2008, *Sol. Phys.*, 247, 269
- November, L. J., & Simon, G. W. 1988, *ApJ*, 333, 427
- Pariat, E., Démoulin, P., & Berger, M. A. 2005, *A&A*, 442, 1105
- Pariat, E., Démoulin, P., & Nindos, A. 2007, *Advances in Space Research*, 39, 1706
- Parker, E. N. 1957, *J. Geophys. Res.*, 62, 509
- Rust, D. M., & Kumar, A. 1996, *ApJ*, 464, L199+
- Santos, J. C., & Bchner, J. 2007, *Astrophysics and Space Sciences Transactions*, 3, 29
- Schrijver, C. J., Derosa, M. L., Metcalf, T. R., Liu, Y., McTiernan, J., Régnier, S., Valori, G., Wheatland, M. S., & Wiegmann, T. 2006, *Sol. Phys.*, 235, 161
- Schrijver, C. J., DeRosa, M. L., Title, A. M., & Metcalf, T. R. 2005, *ApJ*, 628, 501
- Schuck, P. W. 2005, *ApJ*, 632, 53
- . 2006, *ApJ*, 646, 1358
- Stumpf, P. 1911, *Zeitschrift fur Psychologie*, 321, (Translation in Todorovic 1996)
- Sweet, P. A. 1958, *Electromagnetic phenomena in cosmical physics*, Symposium (International Astronomical Union) No. 6 (Cambridge, England: Cambridge University Press), 123
- Török, T., Kliem, B., & Titov, V. S. 2004, *A&A*, 413, L27
- Tian, L., & Alexander, D. 2008, *The Astrophysical Journal*, 673, 532
- Todorovic, D. 1996, *Perception*, 25, 1235
- Wang, A., Wu, S., Liu, Y., & Hathaway, D. 2008, *The Astrophysical Journal Letters*, 674, L57